

Time-Modulated EM Skins for Integrated Sensing and Communications

L. Poli⁽¹⁾, A. Bansal⁽²⁾, G. Oliveri⁽¹⁾⁽³⁾, A. A. Salas-Sanchez⁽¹⁾⁽³⁾, W. Whittow⁽²⁾, and A. Massa⁽¹⁾⁽³⁾⁽⁴⁾⁽⁵⁾⁽⁶⁾

⁽¹⁾ CNIT - "University of Trento" ELEDIA Research Unit

Via Sommarive 9, 38123 Trento - Italy

Website: www.eledia.org/eledia-unitn

⁽²⁾ Wolfson School of Mechanical, Electrical and Manufacturing Engineering, Loughborough University

Epinal Way, LE11 3TU Loughborough, United Kingdom

E-mail: {A.Bansal, W.G.Whittow}@lboro.ac.uk

Website: www.lboro.ac.uk/schools/meme/

⁽³⁾ ELEDIA Research Center (ELEDIA@UniTN - University of Trento)

DICAM - Department of Civil, Environmental, and Mechanical Engineering

Via Mesiano 77, 38123 Trento - Italy

E-mail: {lorenzo.poli, giacomo.oliveri, aaron.salassanchez, andrea.massa}@unitn.it

Website: www.eledia.org/eledia-unitn

⁽⁴⁾ ELEDIA Research Center (ELEDIA@UESTC - UESTC)

School of Electronic Science and Engineering, Chengdu 611731 - China

E-mail: andrea.massa@uestc.edu.cn

Website: www.eledia.org/eledia-uestc

⁽⁵⁾ ELEDIA Research Center (ELEDIA@TSINGHUA - Tsinghua University)

30 Shuangqing Rd, 100084 Haidian, Beijing - China

E-mail: andrea.massa@tsinghua.edu.cn

Website: www.eledia.org/eledia-tsinghua

⁽⁶⁾ School of Electrical Engineering

Tel Aviv University, Tel Aviv 69978 - Israel

E-mail: andrea.massa@eng.tau.ac.il

Website: <https://engineering.tau.ac.il/>

This work has been submitted to the IEEE for possible publication. Copyright may be transferred without notice, after which this version may no longer be accessible.

Time-Modulated EM Skins for Integrated Sensing and Communications

L. Poli, A. Bansal, G. Oliveri, A. A. Salas-Sanchez, W. Whittow, and A. Massa

Abstract

An innovative solution, based on the exploitation of the harmonic beams generated by time-modulated electromagnetic skins (*TM-EMSs*), is proposed for the implementation of integrated sensing and communication (*ISAC*) functionalities in a Smart Electromagnetic Environment (*SEME*) scenario. More in detail, the field radiated by a user terminal, located at an unknown position, is assumed to illuminate a passive *TM-EMS* that, thanks to a suitable modulation of the local reflection coefficients at the meta-atom level of the *EMS* surface, simultaneously reflects towards a receiving base station (*BS*) a “sum” beam and a “difference” one at slightly different frequencies. By processing the received signals and exploiting monopulse radar tracking concepts, the *BS* both localizes the user terminal and, as a by-product, establishes a communication link with it by leveraging on the “sum” reflected beam. Towards this purpose, the arising harmonic beam control problem is reformulated as a global optimization one, which is successively solved by means of an evolutionary iterative approach to determine the desired *TM-EMS* modulation sequence. The results from selected numerical and experimental tests are reported to assess the effectiveness and the reliability of the proposed approach.

Key words: Reconfigurable Passive *EM* Skins; Smart Electromagnetic Environment; Next-Generation Communications; Integrated Sensing and Communications; Space-Time Coding.

1 Introduction and Rationale

In the last few years, the concept of Smart Electromagnetic Environment (*SEME*) has emerged as a revolutionary paradigm to address several major challenges in next-generation wireless communications systems [1]-[5]. The *SEME* vision is based on the idea that the wave propagation properties of outdoor/indoor environments can be tailored to enhance the “quality” of the resulting wireless links [1]-[5]. Towards this end, several technological solutions have been proposed including both static and reconfigurable electromagnetic skins (*EMSs*) [1][6][7]. These latter have been exploited not only for communications, but also for the localization/tracking of users to yield improved quality-of-service (*QoS*) levels as well as to enable advanced wireless planning/deployment [8][9]. As a matter of fact, the use of *EMS* technologies for sensing purposes is widely explored as proved by the long list of recent contributions (see [8]-[11] and the references therein).

It is worth pointing out that the possibility to jointly localize and establish a connection with wireless terminals not in line-of-sight (*NLOS*) is of great practical interest, especially at higher frequencies, owing to the harsh path loss conditions [10]-[12]. This can be accomplished through dedicated *HWs/SWs* that separately implement the two functionalities [13]. Obviously, a more efficient integrated sensing and communications (*ISAC*) solution is preferable for costs and scalability reasons [10]-[13]. Towards this end, an efficient strategy could be that of exploiting the *monopulse radar* concept [14][15][17][18] within the *SEME* scenario. In principle, a traditional monopulse radar is a multi-beam *sensing* system devoted to identify the position of a target [14][15][17]. Such a localization functionality is physically implemented by realizing two separate simultaneous wireless beams: a difference beam, Δ , and a sum beam, Σ [14][15][17]. Dealing with an *ISAC* system, the sum beam can be used not only for localization purposes, but also to establish a *communication* channel with the user terminal.

Adopting the monopulse radar concept in an *ISAC NLOS* scenario needs (i) the terminal to operate as the primary source and not like in radar scenarios where the target is passive, (ii) the *EMS* to reflect the impinging wave from the terminal towards the *BS*, and (iii) the *BS* to distinguish the received power associated to each Σ/Δ beam. Unfortunately, the practical implementation of such an idea is not trivial. As a matter of fact, a straightforward realization of the monopulse

functionality requires the receiving antenna (i.e., the *BS* in the *SEME* case) to be equipped with at least two separate adaptive feeding networks for affording the Σ/Δ beams [10] as in traditional radar monopulse systems. Following this line of reasoning, reconfigurable *EMS*s have been used in combination with multiple antennas to build monopulse *ISAC* systems [10] albeit requiring significant modifications to the *BS* hardware since independent directive antennas and a comparator feed network must be added [10]. Alternatively, reconfigurable *EMS*s have been designed to synthesize either a Σ beam or a Δ beam directed towards the *BS* at different time instants [11], but losing the simultaneous beams generation [11]. Otherwise, simultaneous Σ/Δ beams could be radiated by recurring to the polarization diversity subject to the condition that the user terminal generates dual-polarized signals.

To overcome such limitations, this work proposes a different approach that meets the following guidelines: to enable the simultaneous synthesis of the Σ/Δ beams, while avoiding major hardware modifications to both the *BS* and the user terminal, by borrowing some key concepts from Time Modulated Arrays (*TMA*s) engineering [16][18]-[21]. Let us remember that a *TMA* is an array where the antenna excitations are periodically turned *on* and *off* according to a user-defined time sequence by means of a set of radio-frequency switches [21]. Thanks to the *time-modulation* process, a set of harmonic signals is generated around the carrier frequency [21]. Each harmonic signal is associated to a unique radiation pattern, which is controlled by the array geometry and the modulation sequence [21]. Such a working mechanism enables a wide variety of functionalities in wireless sensing and communications [21]. As for monopulse radars, *TMA*s have been previously and successfully adopted to implement Σ/Δ beams at different harmonic frequencies [18][21]-[23].

To translate similar concepts in the *SEME* context, let us consider time-modulated *EMS*s (*TM-EMS*s) as the corresponding counterpart of *TMA*s. A *TM-EMS* is an artificial passive surface where, instead of modulating the excitations of the array elements as in *TMA*s, the reflection properties of the *EMS* meta-atoms are dynamically modulated (Fig. 1) [21][24]. By leveraging the properties of time-modulated devices, advanced functionalities in terms of reflected harmonic beam generation and control may be synthesized in *TM-EMS*s, as well. Therefore, the development of an innovative solution, based on *TM-EMS*s, for the *ISAC* scenario at hand is

discussed hereinafter. Figure 1 sketches the operation principle of the proposed *ISAC TM-EMS* system. The user terminal, which is in *NLSO* with the *BS*, acts as the source that illuminates the passive *TM-EMS*. Such a *TM-EMS*, thanks to the modulation in time of the surface reflection properties at the meta-atom level, reflects towards the *BS* both a Σ beam at the carrier frequency and a Δ beam at the first harmonic frequency. The *BS* separately collects the power at the carrier frequency, P_{Σ} , and at the first harmonic term, P_{Δ} , to compute the power index ξ ($\xi \triangleq \frac{P_{\Sigma}}{P_{\Delta}}$). According to the monopulse radar rules, the maximization of ξ allows the *BS* to detect the angular position of the user terminal (“sensing”) and, as a byproduct, to establish with him a maximum-gain link (“communication”) thanks to the Σ beam.

Despite the similarities between *TMA*s and *TM-EMS*s, there are several methodological and practical challenges to be addressed before releasing a reliable *ISAC TM-EMS* system. For instance, unlike *TMA*s, the modulation enforced at the meta-atom level is not “on-off”, but it rather involves a change in the local reflection coefficient on the *EMS* area. Moreover, while the feed network of a *TMA* controls the input signal to each antenna, a *TM-EMS* must accommodate for any impinging wave regardless of its incidence angle.

The main innovative contributions of this work then include: (i) the customisation of the *TMA* concepts to the control of time-reconfigurable passive *EMS*s, (ii) the proof of the feasibility of *ISAC* solutions based on *TM-EMS*s and monopulse radar principles without major modifications on the structure of *BS*s/user-terminals, and (iii) the assessment of the proposed *ISAC* system with full-wave numerical simulations as well as experimental measurements on a prototype.

The outline of the paper is as follows. After the description of the proposed *ISAC* system, the design problem at hand is formulated and an iterative procedure for the synthesis of the time-modulation sequence of the *TM-EMS* is detailed (Sect. 2). A set of representative numerical and experimental results is then reported to illustrate the features of the proposed approach as well as to assess its effectiveness in different operative conditions (Sect. 3). Finally, some conclusions and final remarks follow (Sect. 4).

2 Problem Formulation and Time-Modulated *EMS* Design for *ISAC*

Let us consider the scenario in Fig. 1 where a rectangular *TM-EMS*, composed of $P \times Q$ time-modulated meta-atoms and occupying an area Ω , is illuminated by a time-harmonic incident field $\mathbf{E}^{inc}(\mathbf{r})$, generated by the user terminal, which is modeled as a locally plane wave with wave vector $\mathbf{k}^{inc}(\mathbf{r})$, $\mathbf{r} = (x, y, z)$ being the position vector in a Cartesian coordinate system centered on the *EMS* aperture. The instantaneous local reflection tensor $\bar{\bar{\Gamma}}_{pq}(t)$ at the pq -th ($p = 1, \dots, P; q = 1, \dots, Q$) unit cell of the *TM-EMS* is assumed to be time-modulated by means of a digital signal $U_{pq}(t)$ of period T [21]. By denoting with t_{pq}^{on} ($0 \leq t_{pq}^{on} \leq T$) and t_{pq}^{off} ($0 \leq t_{pq}^{off} \leq T$) the switch-on and switch-off instants, respectively, $U_{pq}(t)$ is mathematically described as a rectangular pulse function with values $U_{pq}(t) = 1$ when $t_{pq}^{on} \leq t \leq t_{pq}^{off}$ and $U_{pq}(t) = 0$ otherwise. Accordingly,

$$\bar{\bar{\Gamma}}_{pq}(t) = \bar{\bar{\Gamma}}^{on} U_{pq}(t) + \bar{\bar{\Gamma}}^{off} \tilde{U}_{pq}(t) \quad (1)$$

where $\tilde{U}_{pq}(t) \triangleq 1 - U_{pq}(t)$ and

$$\bar{\bar{\Gamma}}^{on/off} = \begin{bmatrix} \Gamma_{TE}^{on/off} & \Gamma_{TE-TM}^{on/off} \\ \Gamma_{TM-TE}^{on/off} & \Gamma_{TM}^{on/off} \end{bmatrix} \quad (2)$$

is the on/off numerically-computed reflection tensor state, whose on-diagonal entries (i.e., $\Gamma_{TE}^{on/off}$ and $\Gamma_{TM}^{on/off}$) are the *TE/TM* co-polar local reflection coefficients when the cell in the *on/off* state, while the off-diagonal ones (i.e., $\Gamma_{TE-TM}^{on/off}$ and $\Gamma_{TM-TE}^{on/off}$) are the corresponding cross-polar terms [7][26].

Under the local periodicity approximation [6], the electric/magnetic field in a generic point of the *TM-EMS* ($\mathbf{r} \in \Omega$) is given by the following expression [6][25][26]

$$\begin{cases} \mathbf{E}_-(\mathbf{r}, t) = \sum_{p=1}^P \sum_{q=1}^Q \bar{\bar{\Gamma}}_{pq}(t) \cdot \mathbf{E}^{inc}(\mathbf{r}_{pq}) \Pi_{pq}(\mathbf{r}) \\ \mathbf{H}_-(\mathbf{r}, t) = \frac{1}{\eta_0} \mathbf{k}^{inc}(\mathbf{r}) \times \mathbf{E}_-(\mathbf{r}, t) \end{cases} \quad (3)$$

where η_0 is the free-space impedance, \mathbf{r}_{pq} is the barycenter of the pq -th ($p = 1, \dots, P$; $q = 1, \dots, Q$) meta-atom, and $\Pi_{pq}(\mathbf{r})$ is the pq -th pixel basis function.

By exploiting the Love's equivalence principle, the equivalent electric/magnetic current induced on the *EMS* ($\mathbf{r} \in \Omega$) can be computed as follows [6][27]

$$\begin{cases} \mathbf{J}_e(\mathbf{r}, t) = \hat{\mathbf{z}} \times \mathbf{H}_-(\mathbf{r}, t) \\ \mathbf{J}_m(\mathbf{r}, t) = -\hat{\mathbf{z}} \times \mathbf{E}_-(\mathbf{r}, t) \end{cases} \quad (4)$$

and the far-field expression of the field reflected by the *TM-EMS* ($\mathbf{r} \notin \Omega$) at the instant t turns out to be [6][21]

$$\mathbf{E}^{ref}(\mathbf{r}, t) = \frac{jk_0}{4\pi} \frac{\exp(-jk_0 r) \exp(j\omega_0 t)}{r} \int_{\Omega} \hat{\mathbf{z}} \times [\eta_0 \hat{\mathbf{z}} \times \mathbf{J}_e(\mathbf{r}', t) + \mathbf{J}_m(\mathbf{r}', t)] \exp(jk_0 \hat{\mathbf{r}} \cdot \mathbf{r}') d\mathbf{r}' \quad (5)$$

where k_0 is the wavenumber at the carrier frequency f_0 and ω_0 ($\omega_0 \triangleq 2\pi f_0$) is the angular frequency of the carrier.

Because of the pulse periodicity, each pq -th ($p = 1, \dots, P$; $q = 1, \dots, Q$) instantaneous local reflection tensor can be expanded in a Fourier series [21]

$$\bar{\bar{\Gamma}}_{pq}(t) = \sum_{h=-\infty}^{\infty} \bar{\bar{\Gamma}}_{pq}^h \exp\left(jh \frac{2\pi}{T} t\right) \quad (6)$$

where $\bar{\bar{\Gamma}}_{pq}^h$ [$\bar{\bar{\Gamma}}_{pq}^h \triangleq (\bar{\bar{\Gamma}}_{pq}^{on} u_{pq}^h + \bar{\bar{\Gamma}}_{pq}^{off} \tilde{u}_{pq}^h)$] is the h -th harmonic equivalent surface reflection tensor in the pq -th ($p = 1, \dots, P$; $q = 1, \dots, Q$) meta-atom, while $u_{pq}^h \triangleq \frac{1}{T} \int_{-\frac{T}{2}}^{\frac{T}{2}} U_{pq}(t) \exp(-jh \frac{2\pi}{T} t) dt$ and $\tilde{u}_{pq}^h \triangleq \frac{1}{T} \int_{-\frac{T}{2}}^{\frac{T}{2}} \tilde{U}_{pq}(t) \exp(-jh \frac{2\pi}{T} t) dt$.

By substituting (6) in (3), one obtains that

$$\begin{cases} \mathbf{E}_-(\mathbf{r}, t) = \sum_{h=-\infty}^{\infty} \mathbf{E}_-^h \exp(jh \frac{2\pi}{T} t) \\ \mathbf{H}_-(\mathbf{r}, t) = \sum_{h=-\infty}^{\infty} \frac{1}{\eta_0} \mathbf{k}^{inc}(\mathbf{r}) \times \mathbf{E}_-^h \exp(jh \frac{2\pi}{T} t) \end{cases} \quad (7)$$

where

$$\mathbf{E}_-^h(\mathbf{r}) = \sum_{p=1}^P \sum_{q=1}^Q \bar{\bar{\Gamma}}_{pq}^h \cdot \mathbf{E}^{inc}(\mathbf{r}_{pq}) \Pi_{pq}(\mathbf{r}). \quad (8)$$

Thus, the expression (4) can be rewritten in the following harmonic form

$$\begin{cases} \mathbf{J}_e(\mathbf{r}, t) = \sum_{h=-\infty}^{\infty} \mathbf{J}_e^h(\mathbf{r}) \exp(jh\frac{2\pi}{T}t) \\ \mathbf{J}_m(\mathbf{r}, t) = \sum_{h=-\infty}^{\infty} \mathbf{J}_m^h(\mathbf{r}) \exp(jh\frac{2\pi}{T}t) \end{cases} \quad (9)$$

where $\mathbf{J}_e^h(\mathbf{r}) = \hat{\mathbf{z}} \times \frac{1}{\eta_0} \mathbf{k}^{inc}(\mathbf{r}) \times \mathbf{E}_-^h(\mathbf{r})$ and $\mathbf{J}_m^h(\mathbf{r}) = -\hat{\mathbf{z}} \times \mathbf{E}_-^h(\mathbf{r})$.

By replacing (9) in (5), the harmonic expansion of the reflected field ($\mathbf{r} \notin \Omega$) turns out to be

$$\mathbf{E}^{ref}(\mathbf{r}, t) = \sum_{h=-\infty}^{\infty} \mathbf{E}^h(\mathbf{r}) \exp\left[j\left(\omega_0 + h\frac{2\pi}{T}\right)t\right], \quad (10)$$

$\mathbf{E}^h(\mathbf{r})$ being the h -th harmonic term of the reflected field given by

$$\begin{aligned} \mathbf{E}^h(\mathbf{r}) = & \frac{jk_0}{4\pi} \frac{\exp(-jk_0 r)}{r} \hat{\mathbf{z}} \times \hat{\mathbf{z}} \times \sum_{p=1}^P \sum_{q=1}^Q \left(\frac{1}{T} \int_{-\frac{T}{2}}^{\frac{T}{2}} \left\{ \bar{\Gamma}^{on} U_{pq}(t) + \bar{\Gamma}^{off} [1 - U_{pq}(t)] \right\} \exp(-jh\frac{2\pi}{T}t) dt \right) \\ & \int_{\Omega_{pq}} [\hat{\mathbf{z}} \times \mathbf{k}^{inc}(\mathbf{r}') \times \mathbf{E}^{inc}(\mathbf{r}_{pq}) - \mathbf{E}^{inc}(\mathbf{r}_{pq})] \exp(jk_0 \hat{\mathbf{r}} \cdot \mathbf{r}') d\mathbf{r}' \end{aligned} \quad (11)$$

where Ω_{pq} is the support of the pq -th ($p = 1, \dots, P$; $q = 1, \dots, Q$) unit cell of the *TM-EMS*.

The expressions (10)-(11) show that, as expected, the field reflected by a *TM-EMS*, $\mathbf{E}^{ref}(\mathbf{r}, t)$, $\mathbf{r} \notin \Omega$, can be written as a series of harmonic fields, each h -th one, $\mathbf{E}^h(\mathbf{r}, t)$, being spectrally located at the h -th angular frequency ω_h [$\omega_h = (\omega_0 + h\frac{2\pi}{T})$]. This implies that the frequency of each h -th component of the reflected field can be easily controlled by suitably tailoring T , which is of fundamental importance in the *ISAC* scenario at hand since all the harmonic beams of interest must be measured by the receiver (i.e., the *BS*) without relevant updates with respect to the standard one. Moreover, it is worth remarking that the power associated to each h -th harmonic term/beam decreases as the harmonic index h increases, hence only the first harmonic modes can be profitably used [21]. This is not an issue for the proposed *ISAC* system since it is based on a *TM-EMS* that reflects a Σ -beam at the carrier frequency ($h = 0$) and a Δ -beam at the first harmonic component ($h = H = 1$), while all the remaining are not necessary. Furthermore, one can infer from the above derivation (11), that the synthesis of a desired functionality/pattern at the central ($h = 0$) and harmonic ($h \neq 0$) frequencies requires the definition of suitable sequences of switch-on/switch-off instants, which are coded into the time-modulation vector \mathcal{T} ($\mathcal{T} \triangleq \{t_{pq}^{on}, t_{pq}^{off}; p = 1, \dots, P; q = 1, \dots, Q\}$).

Therefore, after defining the cost function $\Phi(\mathcal{T})$ to enforce the desired pattern features at the harmonic beams of interest (i.e., $h = 0, \dots, H$; $H = 1$) as follows [18]

$$\Phi(\mathcal{T}) = \sum_{h=0}^H \int \mathcal{R} \left[|\mathbf{E}^h(\mathbf{r})|^2 - \mathcal{U}^h(\mathbf{r}) \right] d\mathbf{r} + \int \mathcal{R} \left[\mathcal{L}^h(\mathbf{r}) - |\mathbf{E}^h(\mathbf{r})|^2 \right] d\mathbf{r} \quad (12)$$

where $\mathcal{L}^h(\mathbf{r})$ and $\mathcal{U}^h(\mathbf{r})$ are the lower and the upper masks for the h -th ($h = 0, \dots, H$) harmonic pattern, while $\mathcal{R}[\cdot]$ ($\mathcal{R}[\cdot] \triangleq [\cdot] \times \mathcal{H}[\cdot]$, $\mathcal{H}[\cdot]$ being the Heaviside function) is the ramp function, the synthesis problem at hand can be stated as that of determining the optimal time-modulation setup, \mathcal{T}^* , such that $\Phi(\mathcal{T})$ is minimized

$$\mathcal{T}^* = \arg \left\{ \min_{\mathcal{T}} [\Phi(\mathcal{T})] \right\}. \quad (13)$$

While the design of the desired Σ/Δ -beams may be carried out by defining suitable masks $\mathcal{L}^h(\mathbf{r})$ and $\mathcal{U}^h(\mathbf{r})$ and minimizing (12) with respect to \mathcal{T} , the efficiency of the synthesis process can be significantly improved by adding a set of constraints on the switch-on and switch-off time instants to take into account the nature of the desired beams. From the *TMA* theory [18][21], it is well known that a Δ -shaped first ($h = 1$) harmonic beam can be generated by setting $t_{P-p+1,q}^{on} = t_{pq}^{on} + \frac{T}{2}$ ($p = 1, \dots, \frac{P}{2}$; $q = 1, \dots, Q$) in the digital sequences of the $P \times Q$ *TM-EMS* atoms. In other words, a half-period shift between the left and the right portions of the *EMS* aperture automatically enforces the desired deep null in the Δ beam [18]. Thanks to this, the size of \mathcal{T} (i.e., the number of solution descriptors) is reduced from the original $P \times Q \times 2$ real-valued entries to $P \times Q$. Nevertheless, the minimization of (12) is still a challenging task owing to the highly non-linear and multi-minima nature of $\Phi(\mathcal{T})$.

To properly address the complexity of such a global optimization problem, an evolutionary strategy, inspired by the *TMA* design [18] and based on the particle swarm (*PS*) mechanisms [28], is adopted. More in detail, an iterative loop is carried out (ℓ being the iteration index, $\ell = 1, \dots, L$) where at each ℓ -th ($\ell = 1, \dots, L$) iteration, a set of C guess solutions, $\{\mathcal{T}_c^{(\ell)}; c = 1, \dots, C\}$, is updated according to the *PS* evolution mechanisms until either a maximum number of iterations is reached (i.e., $\ell = L$) or the stagnation condition on the optimal value of the cost function, $\mathcal{T}_\ell^{opt} = \arg \left\{ \min_{c=1, \dots, C; \ell=1, \dots, \ell} \left[\Phi \left(\mathcal{T}_c^{(\ell)} \right) \right] \right\}$, holds true [28]. The optimal

TM-EMS control sequence \mathcal{T}^* , given by $\mathcal{T}^* = \arg \left\{ \min_{c=1,\dots,C; \ell=1,\dots,L} \left[\Phi \left(\mathcal{T}_c^{(\ell)} \right) \right] \right\}$, is finally outputted.

For the sake of clarity, it is worthwhile to point out the key differences with respect to the control of a standard *TMA*: (i) unlike a *TMA*, a *TM-EMS* is a passive reconfigurable structure reflecting an external field, $\mathbf{E}^{inc}(\mathbf{r})$, which is not under the control of the *EMS* itself, but it depends on both the position and the type of the user terminal; (ii) the modulation at the meta-atom level in *TM-EMSs* varies the surface reflection coefficient between different states (e.g., $\overline{\Gamma}^{on}/\overline{\Gamma}^{off}$) instead of connecting/disconnecting each antenna from the feed network as in *TMA*s; (iii) the aim of a *TM-EMS* is to yield the anomalous reflection functionality as well as the harmonic beam shaping without exploiting “static excitations” as usually done in *TMA*s [18].

3 Numerical and Experimental Validation

This section is aimed at illustrating the potentialities of the proposed *ISAC* solution as well as to assess the effectiveness of the synthesized *TM-EMSs* with numerical full-wave Ansys HFSS [29] simulations as well as experimental measurements on a prototype.

Let us model the incident field, generated by the user terminal, as a φ -polarized plane wave at the carrier frequency $f_0 = 5.5$ GHz with 1 [V/m] magnitude that impinges on the *EMS* aperture from the direction θ_{inc} ($\varphi_{inc} = 0$). The *TM-EMS* is composed of square unit cells with $0.45 \times 0.45 \lambda^2$ area and the time-modulation period has been chosen equal to $T = 10^{-6}$ [s], while the optimization of the time-modulation vector \mathcal{T} has been carried out according to the state-of-the-art *PS* guidelines [18] by setting a swarm size of $C = 20$ guess solutions, $L = 1000$ iterations, and an inertial weight equal to 0.4, while the social and the cognitive acceleration coefficients have been fixed to 2.0.

3.1 Numerical Results

In the first numerical experiment, the user has been assumed to be along the direction $\theta_{inc} = 40$ [deg] [i.e., $u_{inc} = 0.64$ ($u_{inc} \equiv u_{UT}$) and $v_{inc} = 0.0$ ($v_{inc} \equiv v_{UT}$)], being $v \triangleq \sin \theta \sin \varphi$ and $u \triangleq \sin \theta \cos \varphi$ and connected to a *BS* situated at an angle $\theta_{refl} = -20$ [deg] [i.e., $u_{refl} = 0.34$

($u_{refl} \equiv u_{BS}$) and $v_{refl} = 0.0$ ($v_{refl} \equiv v_{BS}$)] with respect to a $P \times Q = 10 \times 10$ *TM-EMS*. The upper and lower masks for the sum and the difference beams in (12) have been set as in Figs. 2(a)-2(d) with a -10 [dB] sidelobe level. Moreover, the unit cell response (2) has been modeled as an ideally-reflecting structure with 100% efficiency (i.e., $\bar{\Gamma}^{on} = \mathcal{I}$, $\bar{\Gamma}^{off} = -\mathcal{I}$, \mathcal{I} being the identity matrix).

By optimizing the time-modulation vector \mathcal{T}^* according to the synthesis procedure detailed in Sect. 2, the time-modulated *TM-EMS* control sequence turned out to be characterized by the normalized pulse duration τ_{pq} ($\tau_{pq} \triangleq \frac{t_{pq}^{off} - t_{pq}^{on}}{T}$) in Fig. 2(g) and the normalized rising instant \tilde{t}_{pq}^{on} ($\tilde{t}_{pq}^{on} \triangleq \frac{t_{pq}^{on}}{T}$) in Fig. 2(h). The corresponding distributions of the magnitude of the harmonic beams radiated at the carrier, $\mathbf{E}^0(u, v)$, and at the first harmonic, $\mathbf{E}^1(u, v)$, are shown in Fig. 2(e) and Fig. 2(f), respectively. As it can be observed, the *TM-EMS* reflects the field radiated by the user-terminal towards the *BS* with a Σ -pattern at the carrier frequency ($h = 0$) [Fig. 2(e)] and a Δ -pattern at the $h = 1$ harmonic [Fig. 2(f)]. In both cases, the sidelobe distribution appears well controlled with no major secondary lobes.

The effectiveness of the *TM-EMS* design process when varying the position of the *BS* has been assessed next. The plots of the reflected beams when θ_{refl} is varied from the value of the first test case (i.e., $\theta_{refl} = -20$ [deg]) to $\theta_{refl} = -10$ [deg] [i.e., $u_{BS} = 0.17$ and $v_{BS} = 0.0$] [Figs. 3(a)-3(b)] or $\theta_{refl} = 0$ [deg] [i.e., $u_{BS} = v_{BS} = 0.0$] [Figs. 3(c)-3(d)] show that the conceived *ISAC* system is able to reconfigure the reflection status of the *EMS* meta-atoms to adequately accommodate the desired Σ/Δ -beam directions regardless of the *BS* position.

To quantify the robustness of the proposed solution, the plot of the Σ/Δ beam ratio ξ [18],

$$\xi = \frac{|\mathbf{E}^0(\mathbf{r})|^2}{|\mathbf{E}^1(\mathbf{r})|^2} \bigg|_{\theta=\theta_{refl}}, \quad (14)$$

versus θ_{refl} is reported in Fig. 4. Despite the small *EMS* aperture Ω and the unavoidable scan losses caused by its planar nature as well as the fact that the anomalous reflection is directed away from broadside, the value of ξ ranges in the interval $15.4 \leq \xi \leq 24.9$. Such a positive result (i.e., $\xi > 10$) points out that the *TM-EMS* is not constrained to be oriented towards the *BS* for enabling a correct *ISAC* working of the system.

The third numerical experiment has been devoted to investigate the dependence of the *ISAC* performance on the location of the user terminal. Towards this end, the position of the *BS* has been kept fixed at $\theta_{refl} = 0$ [deg] [i.e., $u_{BS} = v_{BS} = 0.0$] while the user direction has been varied within the range 20 [deg] $\leq \theta_{inc} \leq 30$ [deg] (Fig. 5). Also in this case, the plot of ξ versus θ_{inc} [Fig. 5(a)] and the corresponding reflected patterns [Figs. 5(b)-5(e)] assess an effective control of the harmonic beams according to the *ISAC* requirements regardless of the angular position of the user [e.g., Δ -beam ($h = 1$) - Fig. 5(c) and Fig. 5(e)]. However the adjustment of the on/off sequences to compensate for the different incident fields, since the user position changes while θ_{refl} is kept unaltered, yields to a unavoidable non-symmetric distributions of the lobes in the harmonic patterns [e.g., Σ -beam ($h = 0$) - Fig. 5(b) and Fig. 5(d)] even though the pattern masks in (12) are symmetric. Moreover, Figure 5(a) highlights that the resolution accuracy reduces as θ_{inc} and θ_{refl} gets angularly closer (i.e., $\xi = 2$ when $\theta_{inc} = 20$ [deg], while $\xi = 25$ when $\theta_{inc} = 30$ [deg] being $\theta_{refl} = 0$ [deg]).

Previous experiments refer to an architecture that admits an independent setup of t_{pq}^{on} and t_{pq}^{off} at each pq -th ($p = 1, \dots, P$; $q = 1, \dots, Q$) *EMS* unit cell, which may yield to complex control electronics for separating biasing and control lines of each *EMS* switch. The system can be significantly simplified if the scan direction of the reflected beam has to vary only in the horizontal plane. Under such an hypothesis, only a column-wise control of the *TM-EMS* is needed so that $t_{pq}^{on} = t_p^{on}$ and $t_{pq}^{off} = t_p^{off}$ ($q = 1, \dots, Q$; $p = 1, \dots, P$).

Figure 6 is related to the same test case and *EMS* layout ($P \times Q = 10 \times 10$) of Fig. 5, but assuming a column-wise working of the *TM-EMS*. The plot of ξ in Fig. 6(a) proves the effectiveness of the simplified *ISAC* system being $6.9 \leq \xi \leq 17.1$ when 20 [deg] $\leq \theta_{inc} \leq 40$ [deg]. For illustrative purposes, the harmonic reflected patterns, generated by the time-modulated sequences in Fig. 7, when $\theta_{inc} = 40$ [deg] (i.e., $u_{UT} = 0.64$ and $v_{UT} = 0.0$) and $\theta_{inc} = 20$ [deg] (i.e., $u_{UT} = 0.34$ and $v_{UT} = 0.0$) are reported in Figs. 6(b)-6(c) and Figs. 6(d)-6(e), respectively.

The process enabling a passive listening *BS* to detect the position of an unknown user by means of the conceived *TM-EMS*-based system is then illustrated. More specifically, a $P \times Q = 10 \times 10$ column-wise time-controlled *EMS* has been assumed to lie in a scenario where there is a *BS* at

$\theta_{refl} = 0$ that senses the environment to localize a user terminal placed at $\theta_{inc} = 40$ [deg]. Towards this end, the *TM-EMS* has been dynamically reconfigured by sequentially varying the candidate direction $\hat{\theta}_{inc}$ within the range 0 [deg] $\leq \hat{\theta}_{inc} \leq 50$ [deg], while the (fixed) *BS* has been delegated to measure P_{Σ} and P_{Δ} for computing the index ξ in correspondence with each $\hat{\theta}_{inc}$ value. The plot of ξ in Fig. 8(a) shows that, as expected, the power ratio value exhibits a peak when $\hat{\theta}_{inc} = \theta_{inc}$. For completeness, the plots of the corresponding Σ/Δ -beams at representative angular samples $\hat{\theta}_{inc}$ are reported in Fig. 8 along with the corresponding *TM-EMS* time-control sequences. It is interesting to notice that the alignment of the $h = 0$ and $h = 1$ beams towards the *BS* (i.e., $\theta_{refl} = 0 \rightarrow u_{BS} = v_{BS} = 0.0$) is obtained only when $\hat{\theta}_{inc} = \theta_{inc}$ [Figs. 8(j)-8(k)] by setting \mathcal{T}^* as in Figs. 8(l)-8(m). Otherwise [i.e., $\hat{\theta}_{inc} = 0$ [deg] - Figs. 8(b)-8(c); $\hat{\theta}_{inc} = 20$ [deg] - Figs. 8(f)-8(g)], the maximum/null of the sum/difference pattern is not at $u_{BS} = v_{BS} = 0.0$ when $\hat{\theta}_{inc} \neq \theta_{inc}$.

In the subsequent test case, the scalability of the proposed *ISAC* system has been verified by considering a wider *EMS* aperture of $P \times Q = 24 \times 24$ unit cells, while setting $\theta_{inc} = 30$ [deg] (i.e., $u_{UT} = 0.5$ and $v_{UT} = 0.0$) and $\theta_{refl} = 0$ [deg] (i.e., $u_{BS} = v_{BS} = 0.0$). The reflected beams synthesized, after the *PS* optimization, with the time-modulated sequence in Figs. 9(c)-9(d) are shown in Fig. 9(a) ($h = 0$) and Fig. 9(b) ($h = 1$). It can be inferred that the increased area of the *EMS* Ω has been profitably exploited to provide narrower Σ/Δ -beams and well controlled sidelobes [e.g., Fig. 9(b) vs. Fig. 5(c)] notwithstanding the simplified column-wise controlled *TM-EMS*.

The final numerical experiment is aimed at validating the proposed *ISAC* scheme in the presence of a non-ideal *TM-EMS* by emulating the actual micro-scale response of the reconfigurable passive *TM-EMS* with the Ansys HFSS simulator. By considering an FR4 ($\epsilon_r = 4.29$, $\tan \delta = 2.0 \times 10^{-2}$) substrate with 1.6×10^{-3} [m] thickness and the MACOM MADP-000907-14020 diodes as switching devices, the single-bit structure in [7] has been chosen for the *TM-EMS* meta-atom by also including the biasing circuits and RF chokes (Fig. 10). The values of the geometrical descriptors of the unit cell in Fig. 10 are provided in Tab. I. Numerically, the *TM-EMS* has been modeled by using the finite-element boundary-integral (*FE-BI*) method, without periodic boundary conditions approximations or the use of Floquet ports, to take into account

both the internal coupling and the edge diffraction effects of the *TM-EMS* layout.

The Σ/Δ patterns radiated by the $P \times Q = 8 \times 8$ non-ideal *TM-EMS* arrangement in Fig. 11(a) when $\theta_{inc} = 30$ [deg] (i.e., $u_{UT} = 0.5$ and $v_{UT} = 0.0$) and $\theta_{refl} = 0$ [deg] (i.e., $u_{BS} = v_{BS} = 0.0$) are shown in Figs. 11(b)-11(c). It turns out that the *TM-EMS* reflects a well-defined sum pattern at the $h = 0$ harmonic [Fig. 11(b)] and the $h = 1$ difference beam exhibits the desired null along the $\theta_{refl} (\rightarrow u_{BS})$ direction [Fig. 11(c)]. As for the main quantization lobe in the carrier frequency pattern [Fig. 11(b)], it is caused by the specular reflection of the incident beam and it can be reduced/mitigated by adopting a more advanced *EMS* meta-atom design [6][7]. Similar conclusions on the Σ/Δ beam control and sidelobe distribution hold true for the full-wave simulation of a *TM-EMS* featuring a wider *EMS* aperture with $P \times Q = 16 \times 16$ unit cells [Fig. 12(a)].

3.2 Experimental Measurements

A *TM-EMS* prototype has then been manufactured and measured (Fig. 13). More specifically, the optimized $P \times Q = 16 \times 16$ design in Fig. 12(a) with a total area of $\Omega \approx 40 \times 40$ [cm²] has been fabricated by printing the meta-atoms arrangement, including the surface-mounted diodes, on a 1.6×10^{-3} [m]-thick FR4 substrate [Fig. 13(a)], while realizing the biasing lines on a separate 1.0×10^{-4} [m]-thick FR4 substrate (Tab. I) then connected to a Raspberry PI control unit [Fig. 13(b)].

The measurement setup is sketched in Fig. 14(a), while the measurement process has been carried out by using a RF source operating at $f_0 = 5.5$ [GHz] and setting $T = 3.0 \times 10^{-6}$ [s]. In particular, the *TM-EMS* prototype has been mounted on a wooden frame [Fig. 13(b)], coated with a radar absorbing material [Fig. 13(a)], and an Ainfo LB4550 standard gain horn antenna has been used for simulating both the source and the field probe [Fig. 14(b)]. Moreover, the receiving antenna has been mounted on a mechanically rotating platform to automatically collect the reflected pattern samples in the whole azimuth plane [Fig. 14(b)]. Otherwise, the transmitting antenna has been installed on a fixed support located 80 [cm] away from the *TM-EMS* and with a 30 [deg] elevation offset to avoid blockage effects during the scan [Fig. 14(a)]. The plots of the Ansys HFSS-simulated and measured beam patterns at the carrier ($h = 0$)

frequency [Fig. 15(a)] and at the first ($h = 1$) harmonic [Fig. 15(b)] show a satisfactory agreement between numerically-simulated and practically-measurable *TM-EMS* reflection properties at both frequencies. Such a result also experimentally proves the feasibility of an *ISAC* system based on *TM-EMS*s by also assessing its reliability even when the target to be detected is located close to the *EMS* (Fig. 14) and despite the relatively inexpensive fabrication of the prototype featuring a high-loss substrate.

4 Concluding Remarks

The implementation of an *ISAC* system, based on the well-established monopulse radar concepts and exploiting the dynamic control of the harmonic beam-patterns reflected by a *TM-EMS*, has been proposed. The control of the reflected beams features, obtained from the design of the time-modulation sequences of the *TM-EMS*, has been formulated as an optimization problem then solved with a *PS*-driven iterative approach.

From the numerical/experimental results, the following outcomes and accomplishments can be drawn:

- the proposed approach is able to fulfill the requirements of an *ISAC* system in terms of generation of a Σ -beam at the carrier ($h = 0$) and a Δ -beam at the first ($h = 1$) harmonic frequency regardless of the relative angular position of both the user terminal (*source*) and the *BS* base station (*receiver*) (Figs. 4-5);
- the use of simplified *TM-EMS* architectures with a column-wise control (Fig. 7) still guarantees an excellent Σ/Δ -beam control for azimuth-selective sensing and communications functionalities (Fig. 6);
- the feasibility of an *ISAC* system based on *TM-EMS*s is confirmed by both full-wave numerical simulations (Fig. 10) and experimental measurements carried out on a prototype built with a relatively inexpensive HW (Fig. 14).

Future works, beyond the scope of the current manuscript, will be aimed at generalizing the proposed *ISAC* system to multi-bit architectures as well as to include additional functionalities

thanks to a further and deeper exploitation of the non-negligible harmonic terms of the *TM-EMS* reflected field.

Acknowledgements

This work benefited from the networking activities carried out within the Project “ICSC National Centre for HPC, Big Data and Quantum Computing (CN HPC)” funded by the European Union - NextGenerationEU within the PNRR Program (CUP: E63C22000970007), the Project “DICAM-EXC” funded by the Italian Ministry of Education, Universities and Research (MUR) (Departments of Excellence 2023-2027, grant L232/2016), the Project “INSIDE-NEXT - Indoor Smart Illuminator for Device Energization and Next-Generation Communications” funded by the Italian Ministry for Universities and Research within the PRIN 2022 Program (CUP: E53D23000990001), and the Project “AURORA - Smart Materials for Ubiquitous Energy Harvesting, Storage, and Delivery in Next Generation Sustainable Environments” funded by the Italian Ministry for Universities and Research within the PRIN-PNRR 2022 Program, and the Project Partnership on “Telecommunications of the Future” (PE000000001 - program “RESTART”), funded by the European Union under the Italian National Recovery and Resilience Plan (NRRP) of NextGenerationEU (CUP: E63C22002040007). A. Massa wishes to thank E. Vico and L. Massa for the never-ending inspiration, support, guidance, and help.

References

- [1] F. Yang, D. Erricolo, and A. Massa, “Guest Editorial - Smart Electromagnetic Environment,” *IEEE Trans. Antennas Propag.*, vol. 70, no. 10, pp. 8687-8690, Oct. 2022.
- [2] A. Massa, A. Benoni, P. Da Ru, S. K. Goudos, B. Li, G. Oliveri, A. Polo, P. Rocca, and M. Salucci, “Designing smart electromagnetic environments for next-generation wireless communications,” *Telecom*, vol. 2, no. 2, pp. 213-221, 2021.
- [3] M. Di Renzo, A. Zappone, M. Debbah, M.-S. Alouini, C. Yuen, J. De Rosny, and S. Tretyakov, “Smart radio environments empowered by reconfigurable intelligent surfaces:

- How it works, state of research, and the road ahead,” *IEEE J. Sel. Areas Comm.*, vol. 38, no. 11, pp. 2450-2525, Nov. 2020.
- [4] M. Barbuto, Z. Hamzavi-Zarghani, M. Longhi, A. Monti, D. Ramaccia, S. Vellucci, A. Toscano, and F. Bilotti, “Metasurfaces 3.0: a new paradigm for enabling smart electromagnetic environments,” *IEEE Trans. Antennas Propag.*, vol. 70, no. 10, pp. 8883-8897, Oct. 2022.
- [5] M. Di Renzo, M. Debbah, D.-T. Phan-Huy, A. Zappone, M.-S. Alouini, C. Yuen, V. Sciancalepore, G. C. Alexandropoulos, J. Hoydis, H. Gacanin, J. De Rosny, A. Bounceur, G. Lerosey, and M. Fink, “Smart radio environments empowered by reconfigurable AI metasurfaces: An idea whose time has come,” *EURASIP J. Wireless Commun. Net.*, vol. 129, pp. 1-20, 2019.
- [6] G. Oliveri, P. Rocca, M. Salucci, and A. Massa, “Holographic smart EM skins for advanced beam power shaping in next generation wireless environments,” *IEEE J. Multiscale Multiphysics Computat. Techn.*, vol. 6, pp. 171-182, Oct. 2021.
- [7] G. Oliveri, P. Rocca, M. Salucci, D. Erricolo, and A. Massa, “Multi-scale single-bit RP-EMS synthesis for advanced propagation manipulation through System-by-Design,” *IEEE Trans. Antennas Propag.*, vol. 70, no. 10, pp. 8809-8824, Oct. 2022.
- [8] H. Zhang, B. Di, K. Bian, Z. Han, H. V. Poor, and L. Song, “Toward ubiquitous sensing and localization with reconfigurable intelligent surfaces,” *Proc. IEEE*, vol. 110, no. 9, pp. 1401-1422, Sep. 2022.
- [9] J. Hu, H. Zhang, B. Di, L. Li, K. Bian, L. Song, Y. Li, Z. Han, and H. V. Poor, “Reconfigurable intelligent surface based RF sensing: Design, optimization, and implementation,” *IEEE J. Sel. Areas Communic.*, vol. 38, no. 11, pp. 2700-2716, Nov. 2020.
- [10] X. Ma, J. Han, G. Li, M. Chang, Y. Tian, S. Chen, H. Liu, L. Li, T. J. Cui, “A Wideband 1-bit reconfigurable electromagnetic surface for monopulse radar applications,” *IEEE Trans. Antennas Propag.*, vol. 71, no. 6, pp. 5475-5480, Jun. 2023.

- [11] X. Wan, Q. Xiao, Y. Z. Zhang, Y. Li, J. Eisenbeis, J. W. Wang, Z. A. Huang, H. X. Liu, T. Zwick, and T. J. Cui, "Reconfigurable sum and difference beams based on a binary programmable metasurface," *IEEE Antennas Wireless Propag. Lett.*, vol. 20, no. 3, pp. 381-385, Mar. 2021.
- [12] M. Z. Chowdhury, M. Shahjalal, S. Ahmed, and Y. M. Jang, "6G wireless communication systems: Applications, requirements, technologies, challenges, and research directions," *IEEE Open J. Commun. Soc.*, vol. 1, pp. 957-975, 2020.
- [13] C. Sturm and W. Wiesbeck, "Waveform design and signal processing aspects for fusion of wireless communications and radar sensing," *Proc. IEEE*, vol. 99, no. 7, pp. 1236-1259, Jul. 2011.
- [14] L. Manica, P. Rocca, A. Martini, and A. Massa, "An innovative approach based on a tree-searching algorithm for the optimal matching of independently optimum sum and difference excitations," *IEEE Trans. Antennas Propag.*, vol. 56, no. 1, pp. 58-66, Jan. 2008.
- [15] P. Rocca, L. Manica, R. Azaro, and A. Massa, "A hybrid approach for the synthesis of sub-arrayed monopulse linear arrays," *IEEE Trans. Antennas Propag.*, vol. 57, no. 1, pp. 280-283, Jan. 2009.
- [16] S. Yang and Z. Nie, "A review of the four dimensional antenna arrays," *J. Electron. Sci. Technol. China*, vol. 4, no. 3, pp. 193-201, Sep. 2006.
- [17] L. Manica, P. Rocca, and A. Massa, "Design of subarrayed linear and planar array antennas with SLL control based on an excitation matching approach," *IEEE Trans. Antennas Propag.*, vol. 57, no. 6, pp. 1684-1691, Jun. 2009.
- [18] L. Poli, P. Rocca, G. Oliveri, and A. Massa, "Harmonic beamforming in time-modulated linear arrays," *IEEE Trans. Antennas Propag.*, vol. 59, no. 7, pp. 2538-2545, Jul. 2011.
- [19] L. Poli, P. Rocca, L. Manica, and A. Massa, "Handling sideband radiations in time-modulated arrays through particle swarm optimization," *IEEE Trans. Antennas Propag.*, vol. 58, no. 4, pp. 1408-1411, Apr. 2010.

- [20] P. Rocca, L. Poli, G. Oliveri, and A. Massa, "Synthesis of time-modulated planar array with controlled harmonic radiations," *J. Electromagn. Waves Appl.*, vol. 24, no. 4, pp. 827-838, 2010.
- [21] P. Rocca, F. Yang, L. Poli, and S. Yang, "Time-modulated array antennas: Theory, techniques, and applications", *J. Electromagn. Waves Applic.*, vol. 33, no. 12, pp. 1503-1531, 2019.
- [22] P. Rocca, L. Manica, L. Poli, and A. Massa, "Synthesis of compromise sum-difference arrays through time-modulation," *IET Radar Sonar Navig.*, vol. 3, no. 6, pp. 630-637, Nov. 2009.
- [23] P. Rocca, L. Poli, L. Manica, and A. Massa, "Synthesis of monopulse time-modulated planar arrays with controlled sideband radiation," *IET Radar, Sonar Navig.*, vol. 6, no. 6, pp. 432-442, 2012.
- [24] L. Zhang, X. Q. Chen, S. Liu, Q. Zhang, J. Zhao, J. Y. Dai, G. D. Bai, X. Wan, Q. Cheng, G. Castaldi, V. Galdi, and T. J. Cui, "Space-time-coding digital metasurfaces," *Nature Communications*, vol. 9, Article No. 4334, pp. 1-11, 2018.
- [25] F. S. Cuesta, I. A. Faniayeu, V. S. Asadchy, and S. A. Tretyakov, "Planar broadband Huygens' metasurfaces for wave manipulations," *IEEE Trans. Antennas Propag.*, vol. 66, no. 12, pp. 7117-7127, Dec. 2018.
- [26] F. Yang and Y. Rahmat-Samii, *Surface Electromagnetics with Applications in Antenna, Microwave, and Optical Engineering*, Cambridge, UK: Cambridge University Press, 2019.
- [27] C. A. Balanis, *Advanced Engineering Electromagnetics*, New York, NY: John Wiley and Sons, 1989.
- [28] P. Rocca, M. Benedetti, M. Donelli, D. Franceschini, and A. Massa, "Evolutionary optimization as applied to inverse problems," *Inv. Probl.*, vol. 25, art no. 123003, pp. 1-41, Dec. 2009.

[29] ANSYS Electromagnetics Suite - HFSS (2021). ANSYS, Inc.

FIGURE CAPTIONS

- **Figure 1.** *Problem Scenario* - Sketch of the proposed ISAC system.
- **Figure 2.** *Illustrative Example (Ideal Meta-Atom, $P \times Q = 10 \times 10$, $\theta_{inc} = 40$ [deg], $\theta_{refl} = -20$ [deg])* - Plots of (a)(b) the lower masks, (c)(d) upper masks, and (e)(f) reflected power patterns at (a)(c)(e) the central frequency ($h = 0$) and (b)(d)(f) the first ($h = 1$) harmonic term along with the corresponding (g) τ_{pq} and (h) \tilde{t}_{pq}^{on} sets.
- **Figure 3.** *Numerical Analysis (Ideal Meta-Atom, $P \times Q = 10 \times 10$, $\theta_{inc} = 40$ [deg])* - Plots of reflected power patterns at (a)(c) the carrier ($h = 0$) and (b)(d) the first ($h = 1$) harmonic frequency when (a)(b) $\theta_{refl} = -10$ [deg] and (c)(d) $\theta_{refl} = 0$ [deg].
- **Figure 4.** *Numerical Analysis (Ideal Meta-Atom, $P \times Q = 10 \times 10$, $\theta_{inc} = 40$ [deg])* - Plot of ξ versus θ_{refl} .
- **Figure 5.** *Numerical Analysis (Ideal Meta-Atom, $P \times Q = 10 \times 10$, $\theta_{refl} = 0$ [deg])* - Plots of (a) ξ versus θ_{inc} and of the reflected power patterns at (b)(d) the carrier frequency ($h = 0$) and (c)(e) the first ($h = 1$) harmonic when (b)(c) $\theta_{inc} = 30$ [deg] and (d)(e) $\theta_{inc} = 20$ [deg].
- **Figure 6.** *Numerical Analysis (Ideal Meta-Atom, $P \times Q = 10 \times 10$, $\theta_{refl} = 0$ [deg], column-wise control)* - Plots of (a) ξ versus θ_{inc} and of the reflected power patterns at (b)(d) the carrier frequency ($h = 0$) and (c)(e) the first ($h = 1$) harmonic when (b)(c) $\theta_{inc} = 40$ [deg] and (d)(e) $\theta_{inc} = 20$ [deg].
- **Figure 7.** *Numerical Analysis (Ideal Meta-Atom, $P \times Q = 10 \times 10$, $\theta_{refl} = 0$ [deg], column-wise control)* - Plots of (a)(c) τ_{pq} and (b)(d) \tilde{t}_{pq}^{on} when (a)(b) $\theta_{inc} = 40$ [deg] and (c)(d) $\theta_{inc} = 20$ [deg].
- **Figure 8.** *Numerical Analysis (Ideal Meta-Atom, $P \times Q = 10 \times 10$, $\theta_{refl} = 0$ [deg], column-wise control, $\theta_{inc} = 40$ [deg])* - Plots of (a) ξ versus $\hat{\theta}_{inc}$ and of reflected power patterns at (b)(f)(j) the carrier frequency ($h = 0$), (c)(g)(k) the first ($h = 1$) harmonic

along with the corresponding $(d)(h)(l) \tau_{pq}$ and $(e)(i)(m) \tilde{t}_{pq}^{on}$ values when $(b)(c)(d)(e) \hat{\theta}_{inc} = 0$ [deg], $(f)(g)(h)(i) \hat{\theta}_{inc} = 20$ [deg], and $(j)(k)(l)(m) \hat{\theta}_{inc} = 40$ [deg].

- **Figure 9.** *Numerical Analysis (Ideal Meta-Atom, $P \times Q = 24 \times 24$, $\theta_{inc} = 30$ [deg], $\theta_{refl} = 0$ [deg], column-wise control)* - Plots of reflected power patterns at (a) the carrier ($h = 0$) and (b) the first ($h = 1$) harmonic along with the corresponding (c) τ_{pq} and (d) \tilde{t}_{pq}^{on} values.
- **Figure 10.** *Numerical Analysis (HFSS Full-wave Modeling)* - Meta-atom geometry: (a) top view, (b) side view, and (c) bottom view.
- **Figure 11.** *Numerical Analysis (HFSS Full-wave Modeling, $P \times Q = 8 \times 8$, $\theta_{inc} = 30$ [deg], $\theta_{refl} = 0$ [deg], column-wise control)* - Sketch of (a) the full-wave model of the *TM-EMS* and plots of (b)(c) the reflected power patterns at (b) the carrier ($h = 0$) and (c) the first ($h = 1$) harmonic.
- **Figure 12.** *Numerical Analysis (HFSS Full-wave Modeling, $P \times Q = 16 \times 16$, $\theta_{inc} = 30$ [deg], $\theta_{refl} = 0$ [deg], column-wise control)* - Sketch of (a) the full-wave model of the *TM-EMS* architecture and plots of (b)(c) reflected power patterns at (b) the carrier ($h = 0$) and (c) the first ($h = 1$) harmonic.
- **Figure 13.** *Experimental Results ($P \times Q = 16 \times 16$, $\theta_{inc} = 30$ [deg], $\theta_{refl} = 0$ [deg], column-wise control)* - Photo of the (a) front and (b) back of the *TM-EMS* prototype as installed within the measurement setup.
- **Figure 14.** *Experimental Results ($P \times Q = 16 \times 16$, $\theta_{inc} = 30$ [deg], $\theta_{refl} = 0$ [deg], column-wise control)* - Measurement setup: (a) logical sketch and (b) photo.
- **Figure 15.** *Experimental Results ($P \times Q = 16 \times 16$, $\theta_{inc} = 30$ [deg], $\theta_{refl} = 0$ [deg], column-wise control)* - Plots of the measured reflected power patterns at (a) the carrier ($h = 0$) and (b) the first ($h = 1$) harmonic.

TABLE CAPTIONS

- **Table I.** *Numerical Validation* - Meta-atom descriptors.

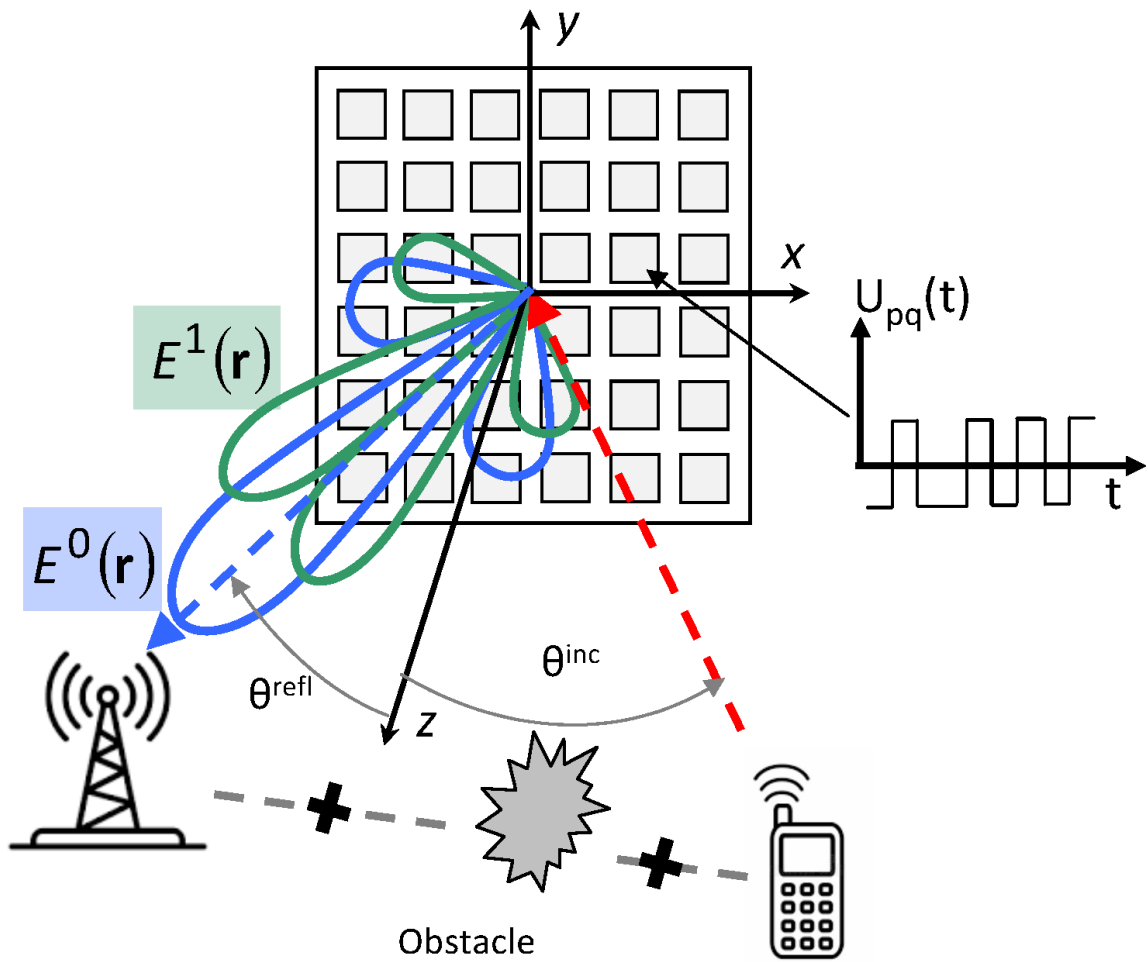


Fig. 1 - L. Poli *et al.*, “Time-Modulated EM Skins for Integrated ...”

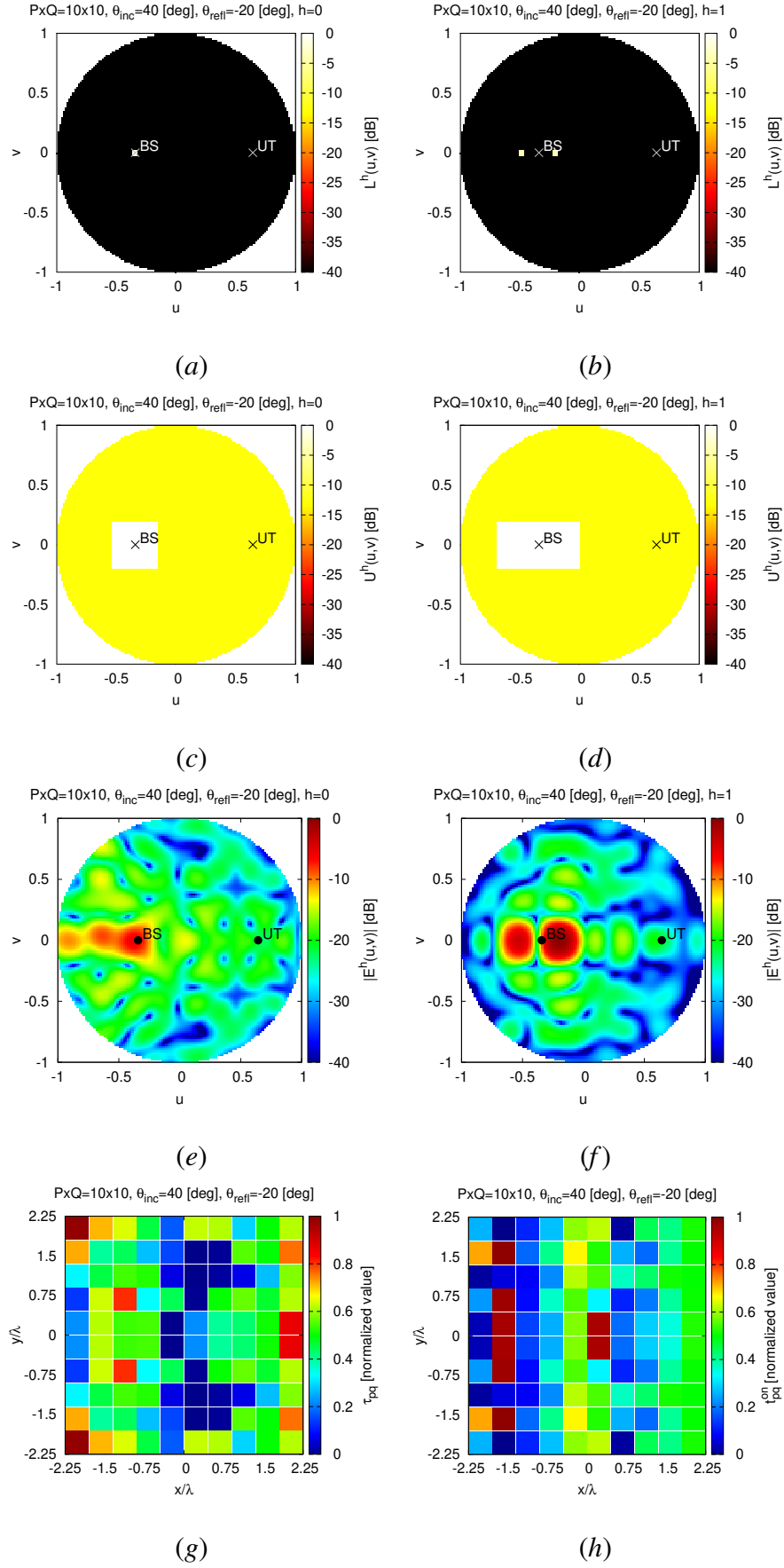


Fig. 2 - L. Poli *et al.*, “Time-Modulated EM Skins for Integrated ...”

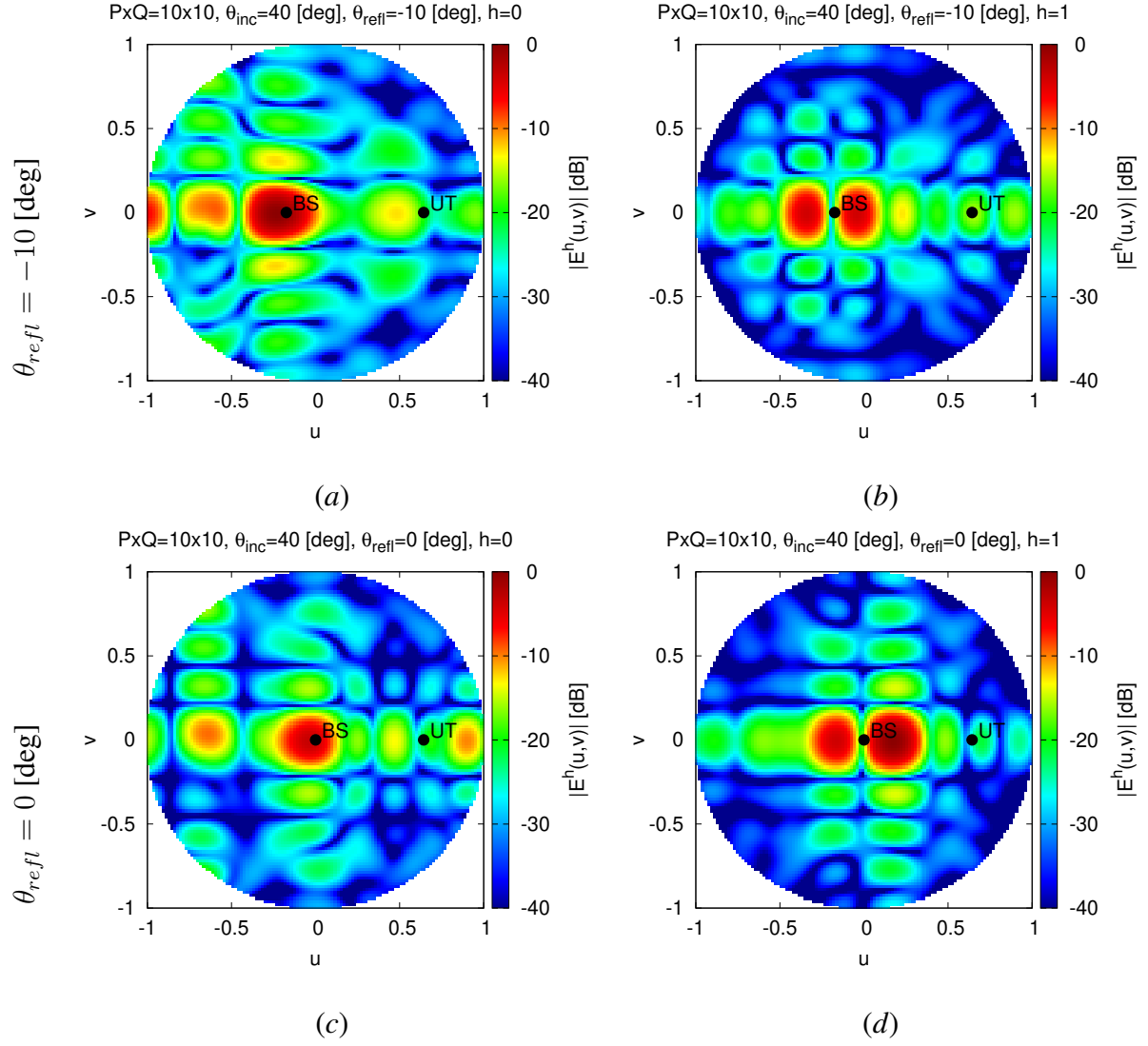


Fig. 3 - L. Poli *et al.*, “Time-Modulated EM Skins for Integrated ...”

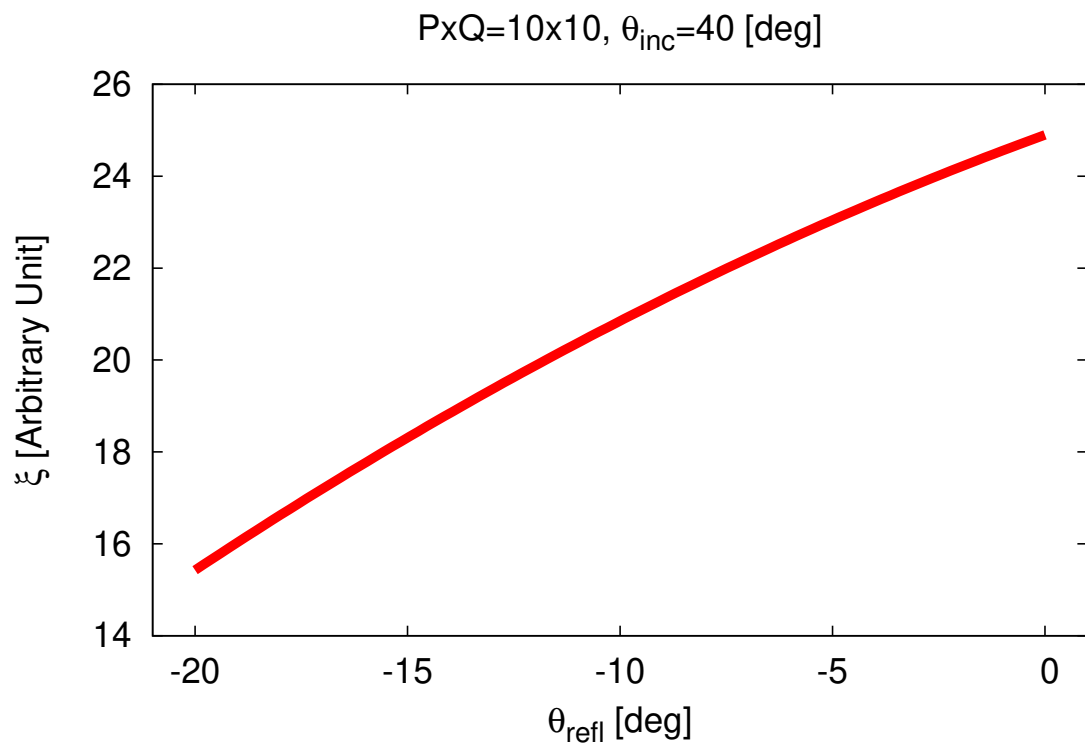


Fig. 4 - L. Poli *et al.*, “Time-Modulated EM Skins for Integrated ...”

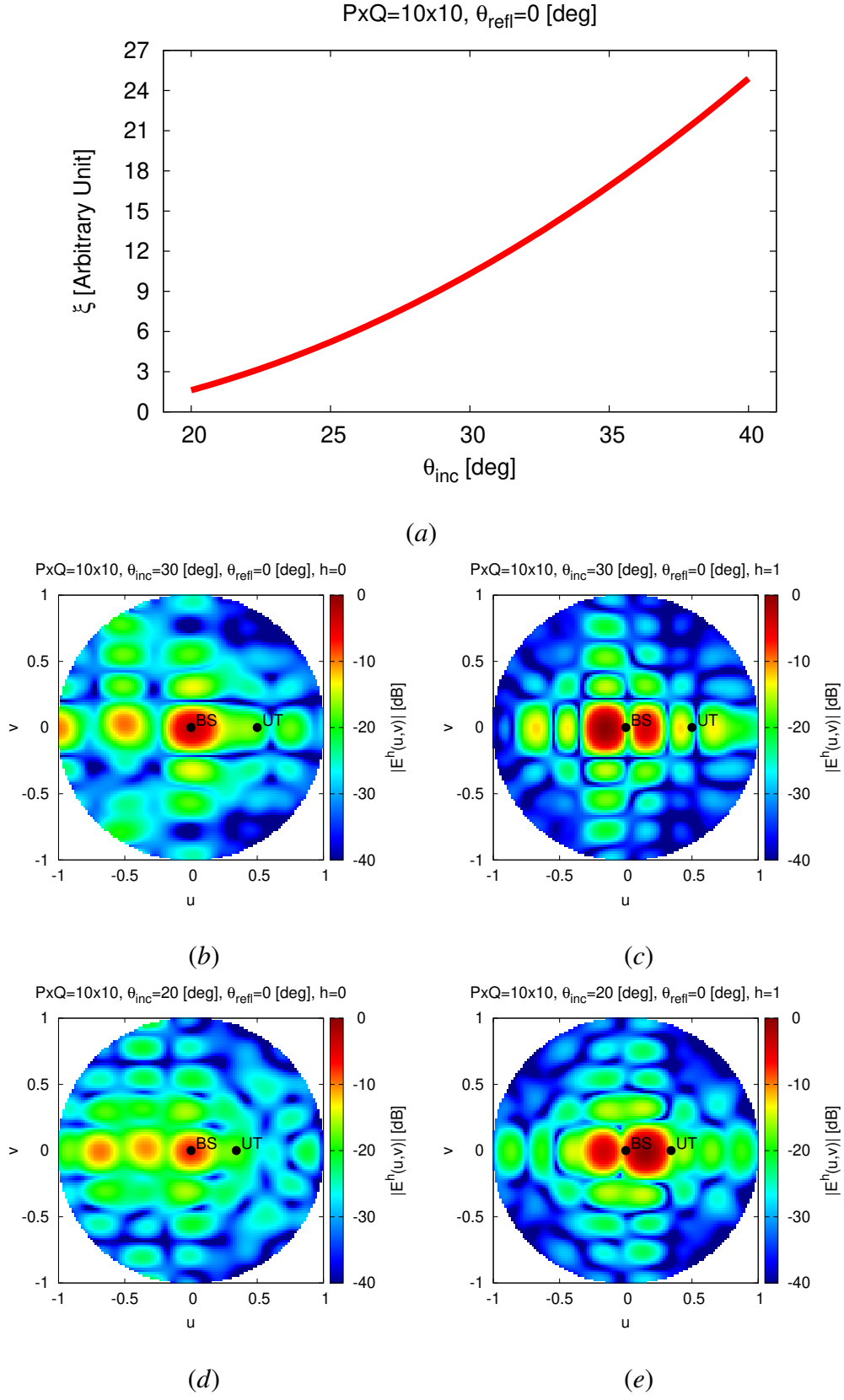


Fig. 5 - L. Poli *et al.*, “Time-Modulated EM Skins for Integrated ...”

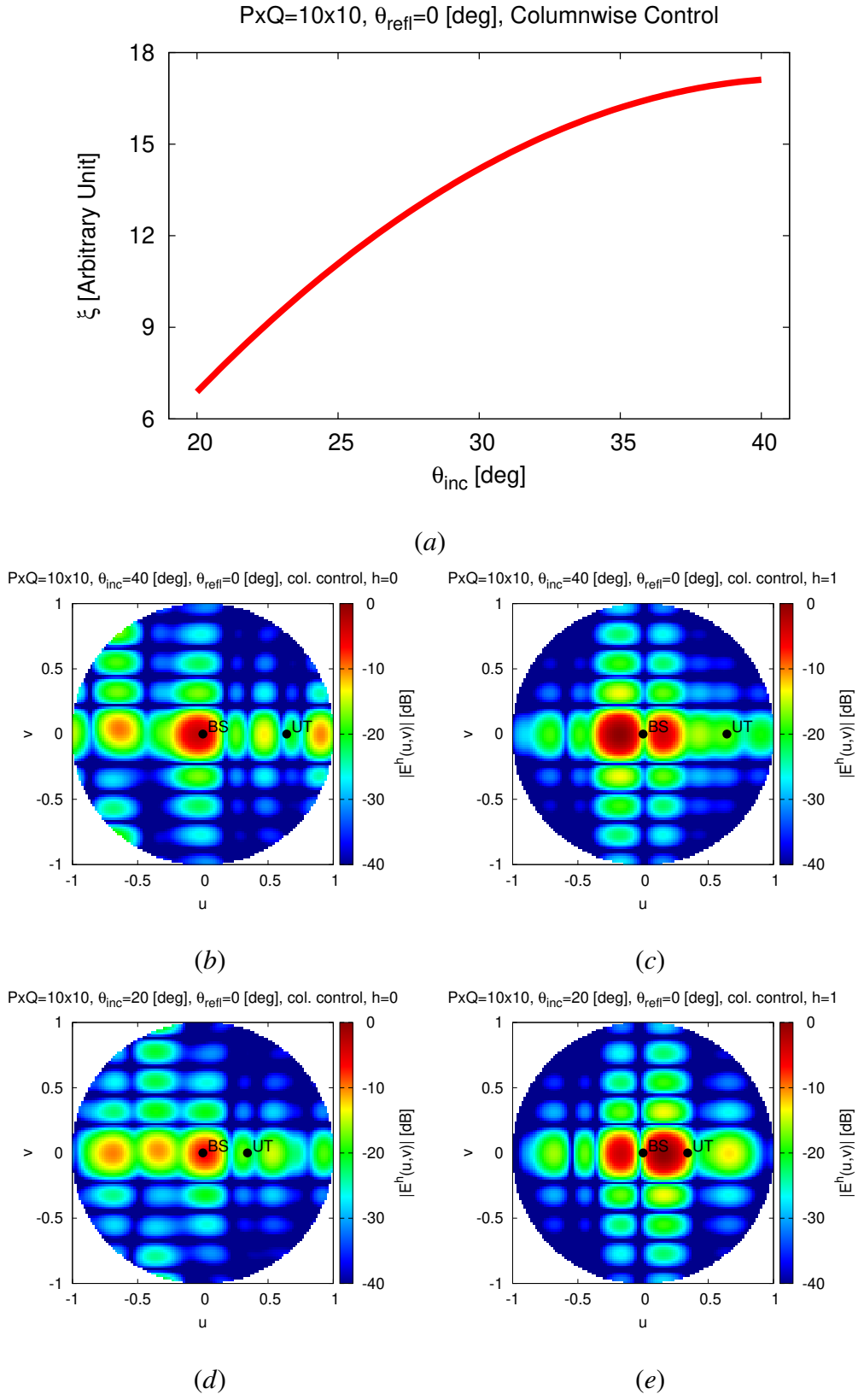


Fig. 6 - L. Poli *et al.*, “Time-Modulated EM Skins for Integrated ...”

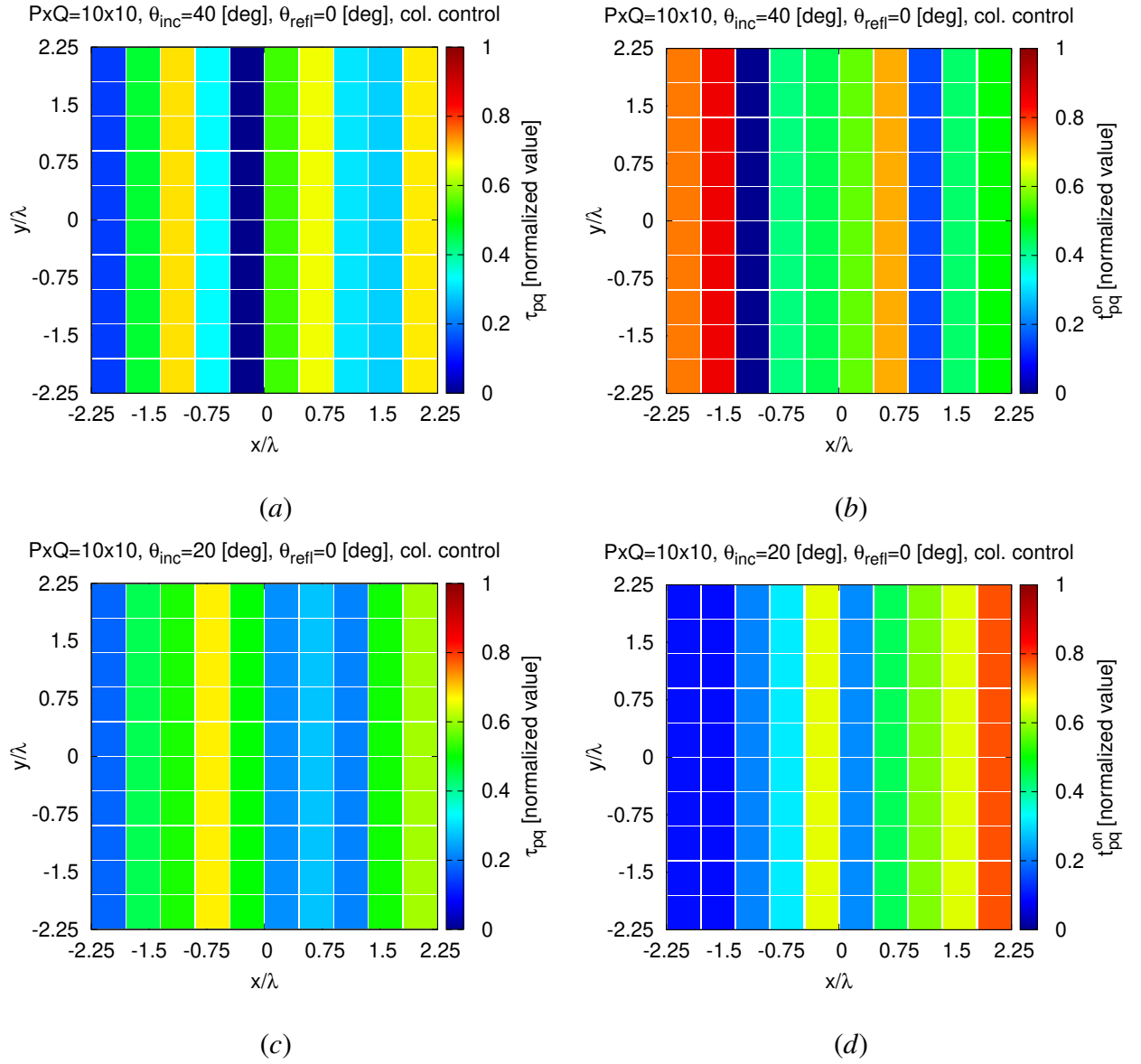


Fig. 7 - L. Poli *et al.*, “Time-Modulated EM Skins for Integrated ...”

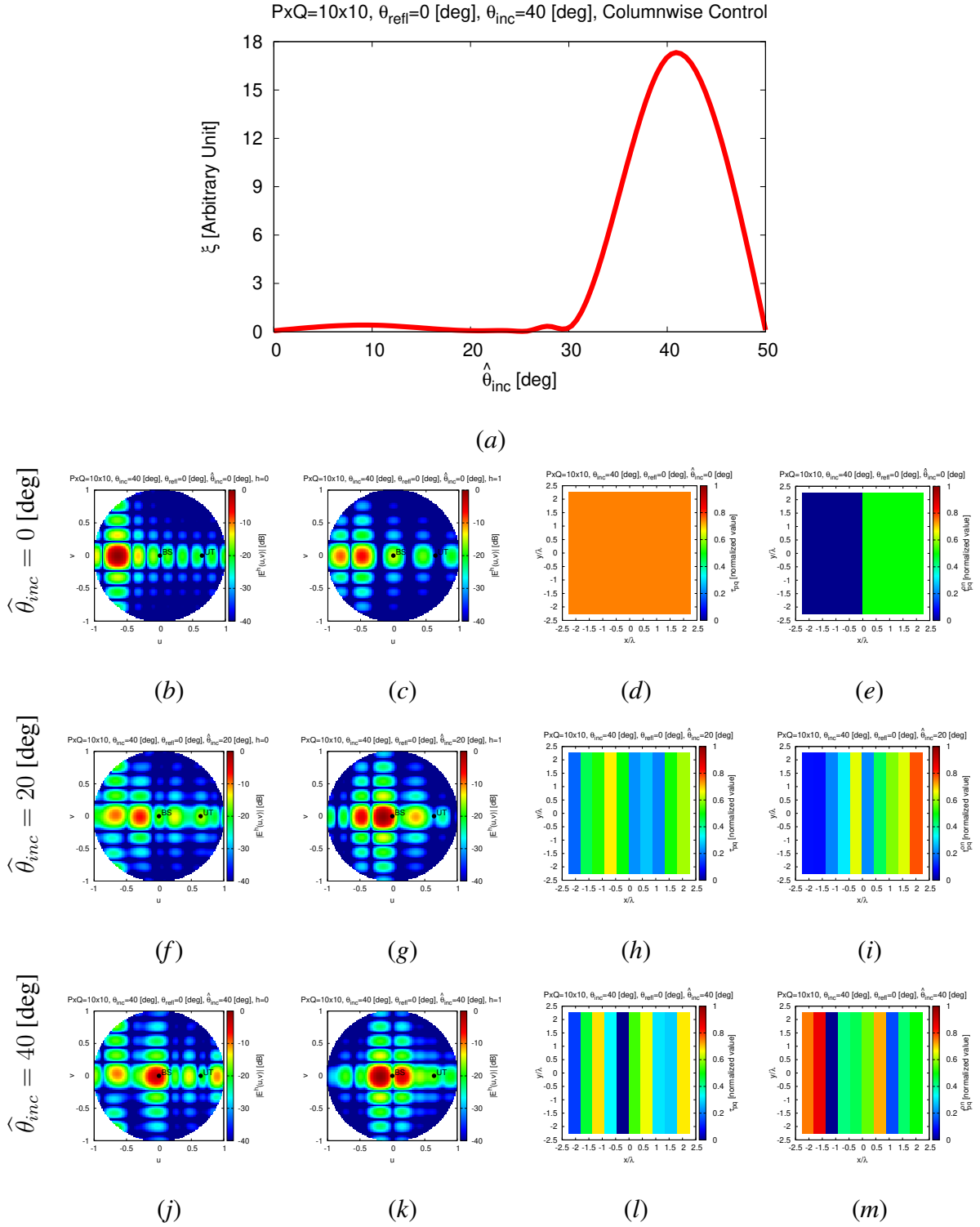
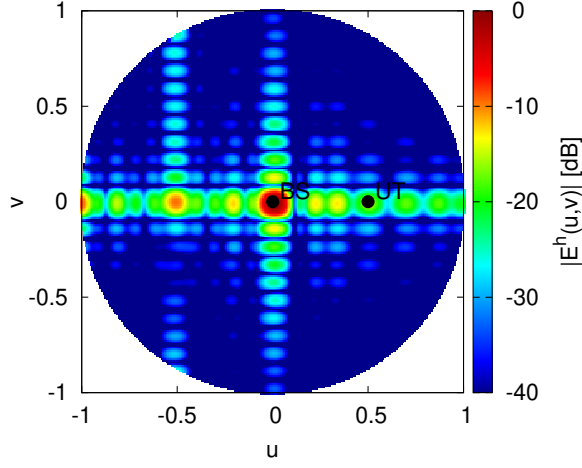


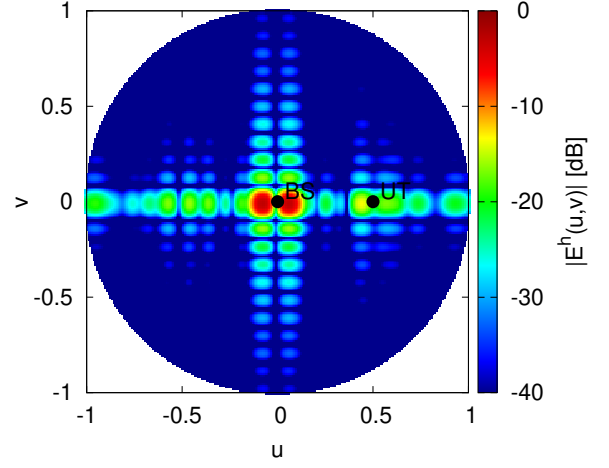
Fig. 8 - L. Poli *et al.*, “Time-Modulated EM Skins for Integrated ...”

PxQ=24x24, $\theta_{\text{inc}}=30$ [deg], $\theta_{\text{refl}}=0$ [deg], col. control, $h=0$



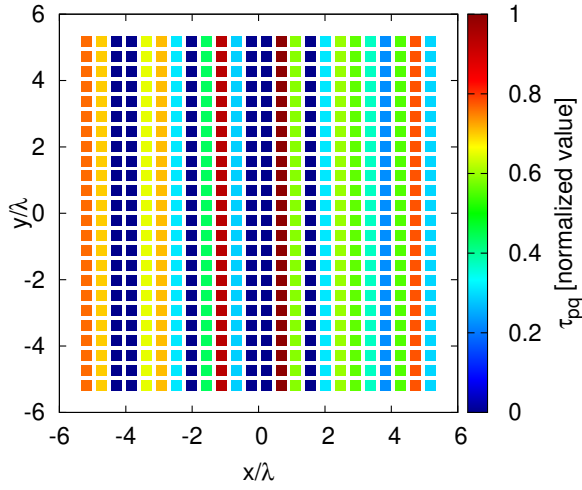
(a)

PxQ=24x24, $\theta_{\text{inc}}=30$ [deg], $\theta_{\text{refl}}=0$ [deg], col. control, $h=1$



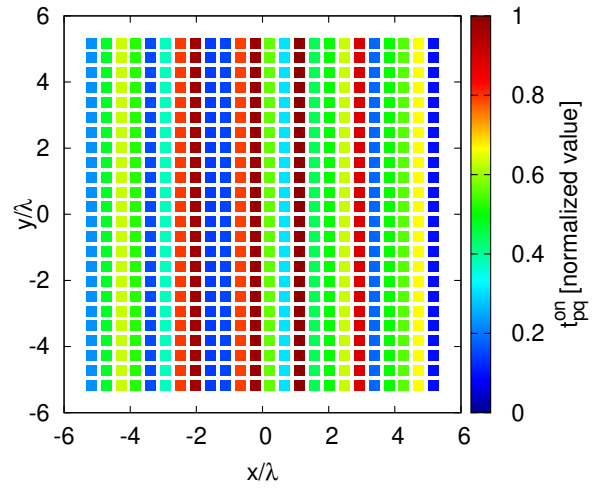
(b)

PxQ=24x24, $\theta_{\text{inc}}=30$ [deg], $\theta_{\text{refl}}=0$ [deg], col. control



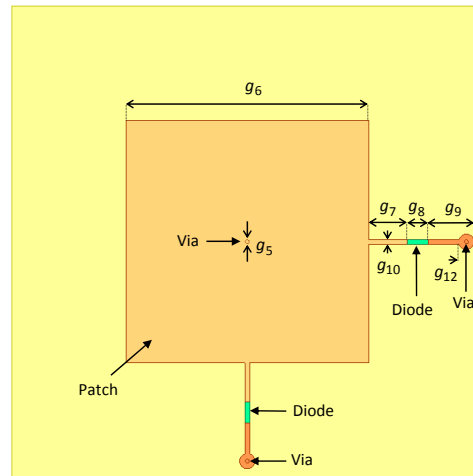
(c)

PxQ=24x24, $\theta_{\text{inc}}=30$ [deg], $\theta_{\text{refl}}=0$ [deg], col. control

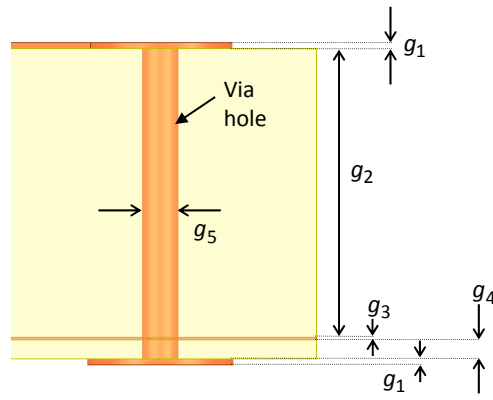


(d)

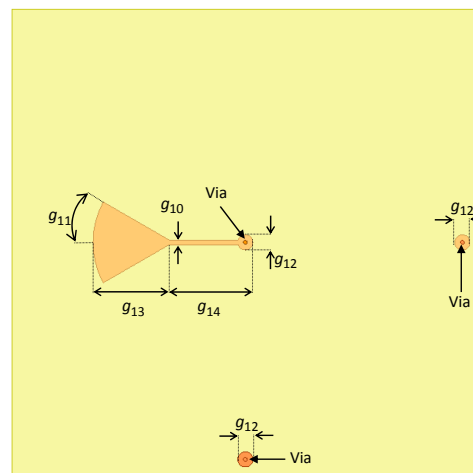
Fig. 9 - L. Poli *et al.*, “Time-Modulated EM Skins for Integrated ...”



(a)

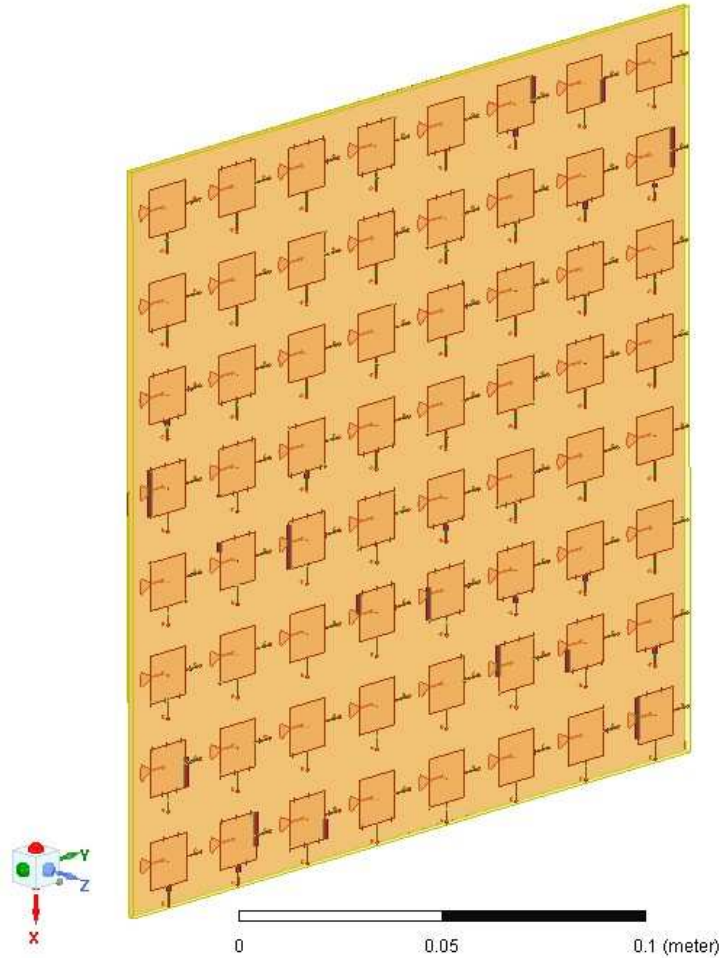


(b)

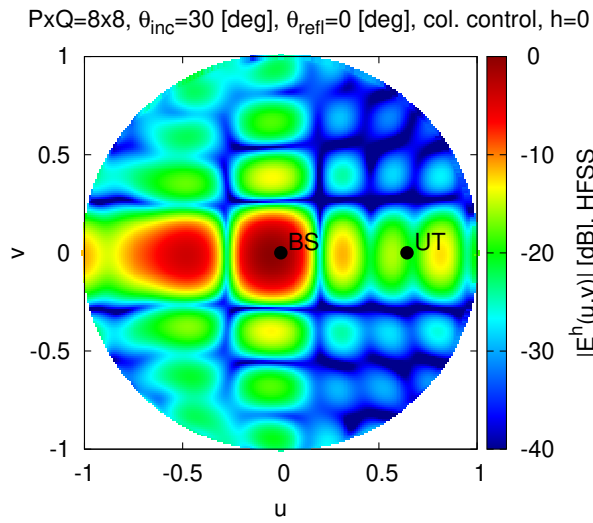


(c)

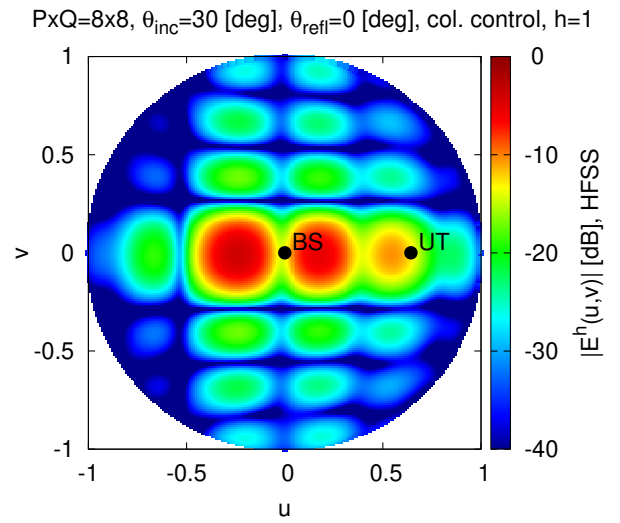
Fig. 10 - L. Poli *et al.*, "Time-Modulated EM Skins for Integrated ..."



(a)



(b)



(c)

Fig. 11 - L. Poli *et al.*, “Time-Modulated EM Skins for Integrated ...”

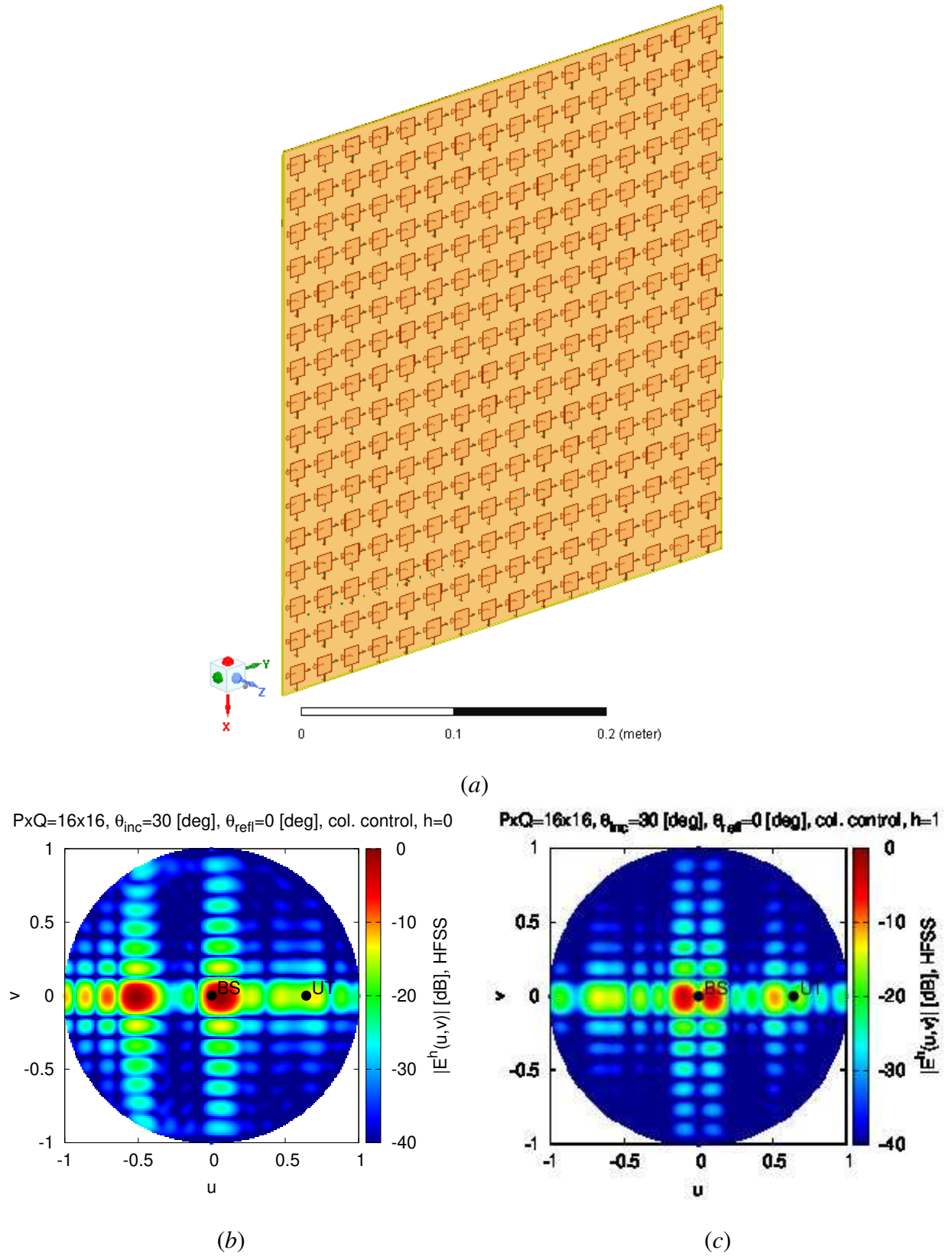
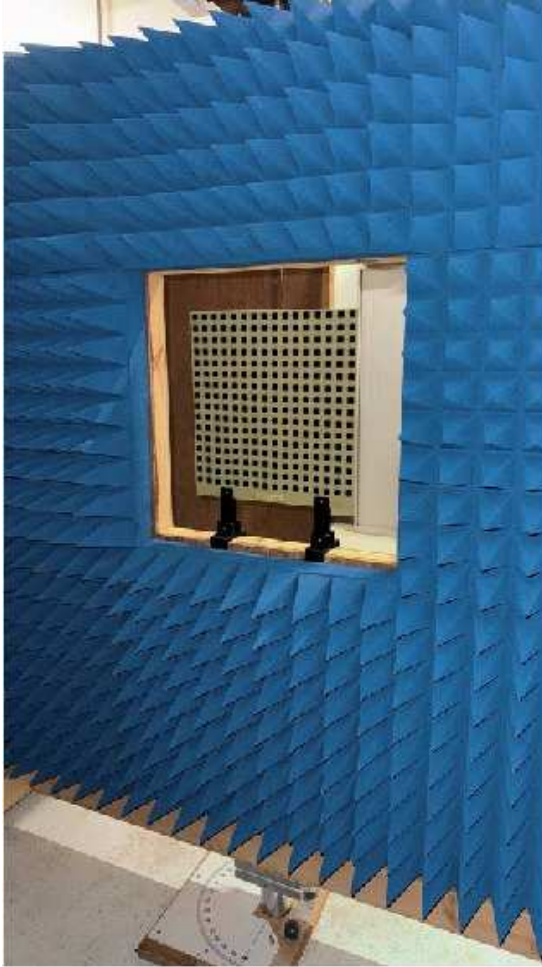
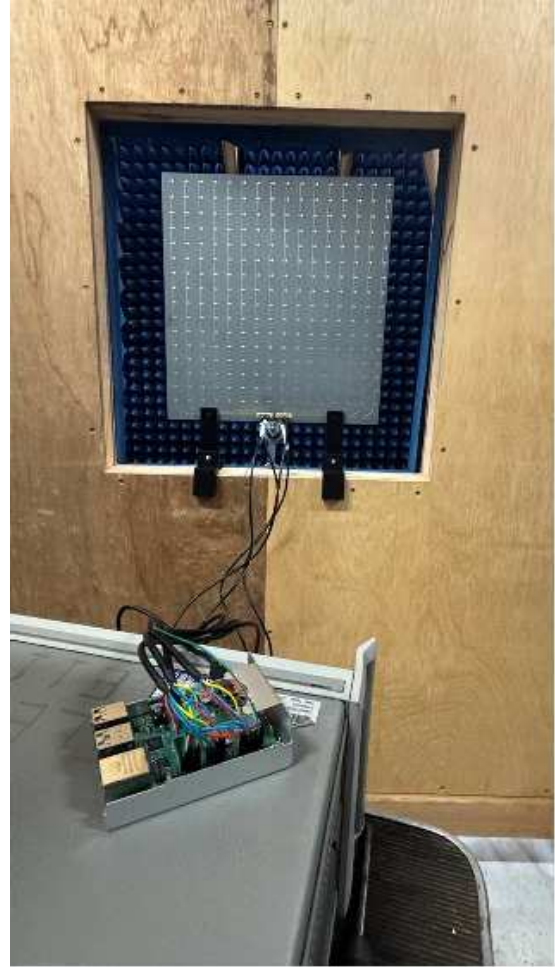


Fig. 12 - L. Poli *et al.*, “Time-Modulated EM Skins for Integrated ...”

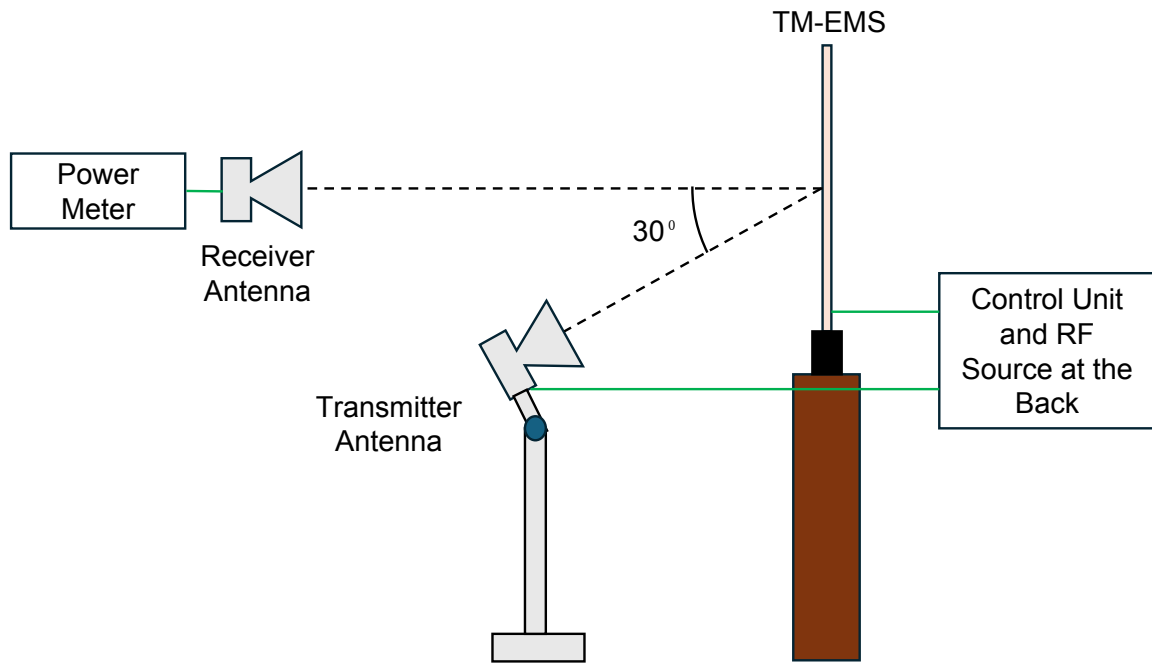


(a)

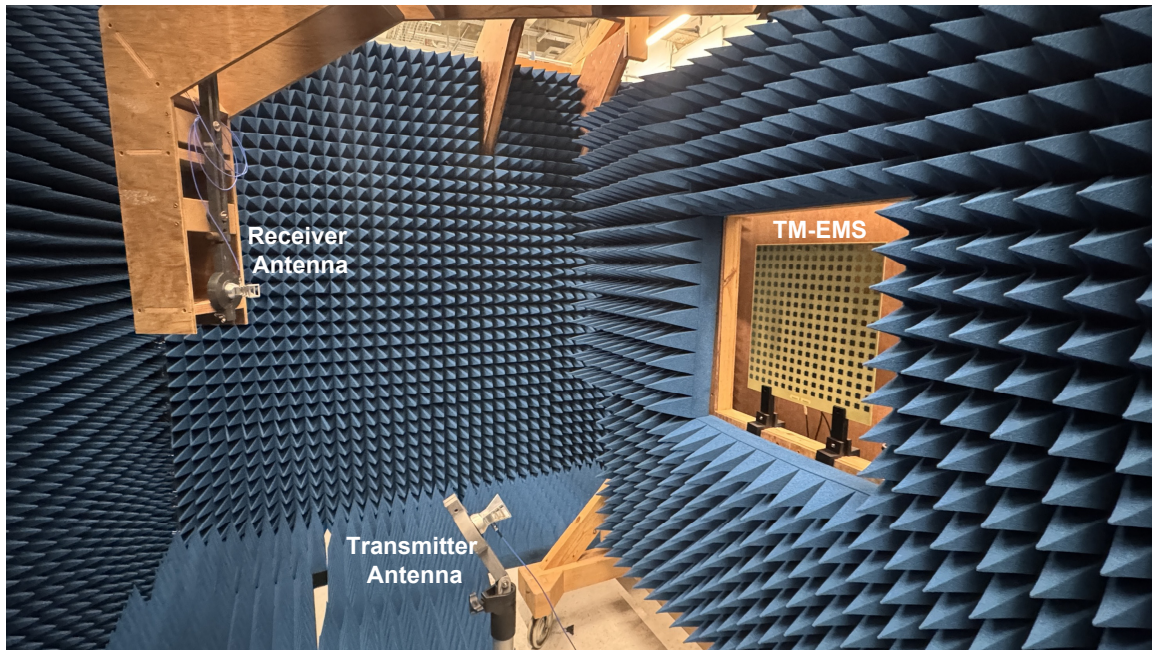


(b)

Fig. 13 - L. Poli *et al.*, “Time-Modulated EM Skins for Integrated ...”



(a)



(b)

Fig. 14 - L. Poli *et al.*, “Time-Modulated EM Skins for Integrated ...”

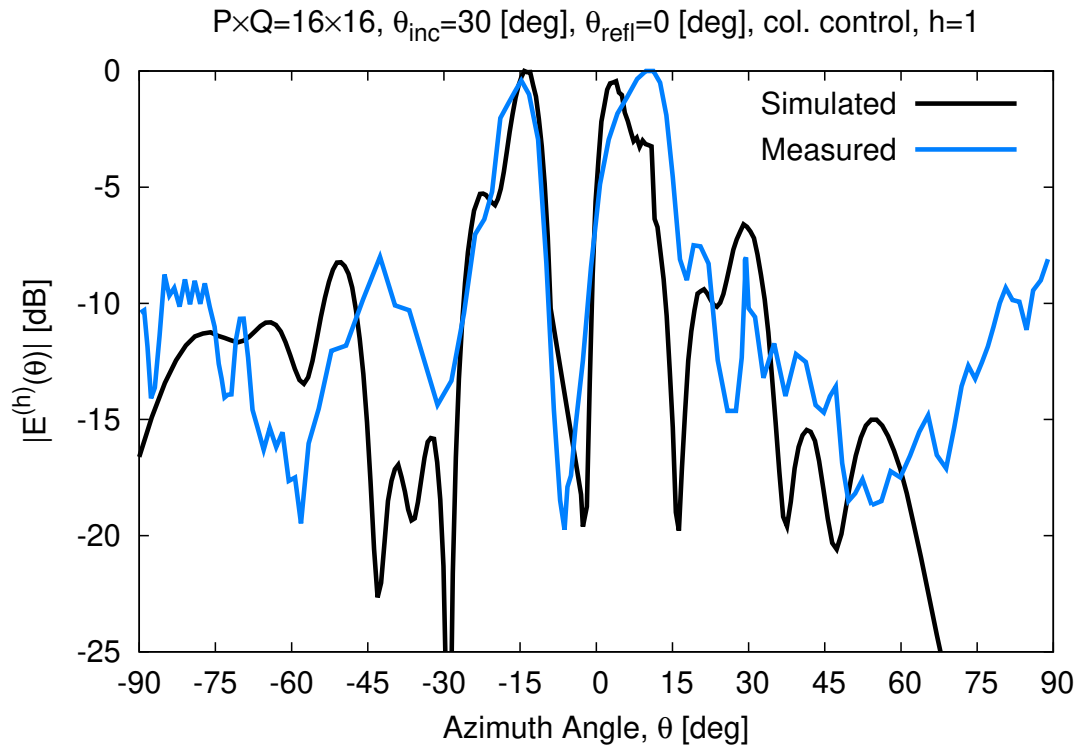
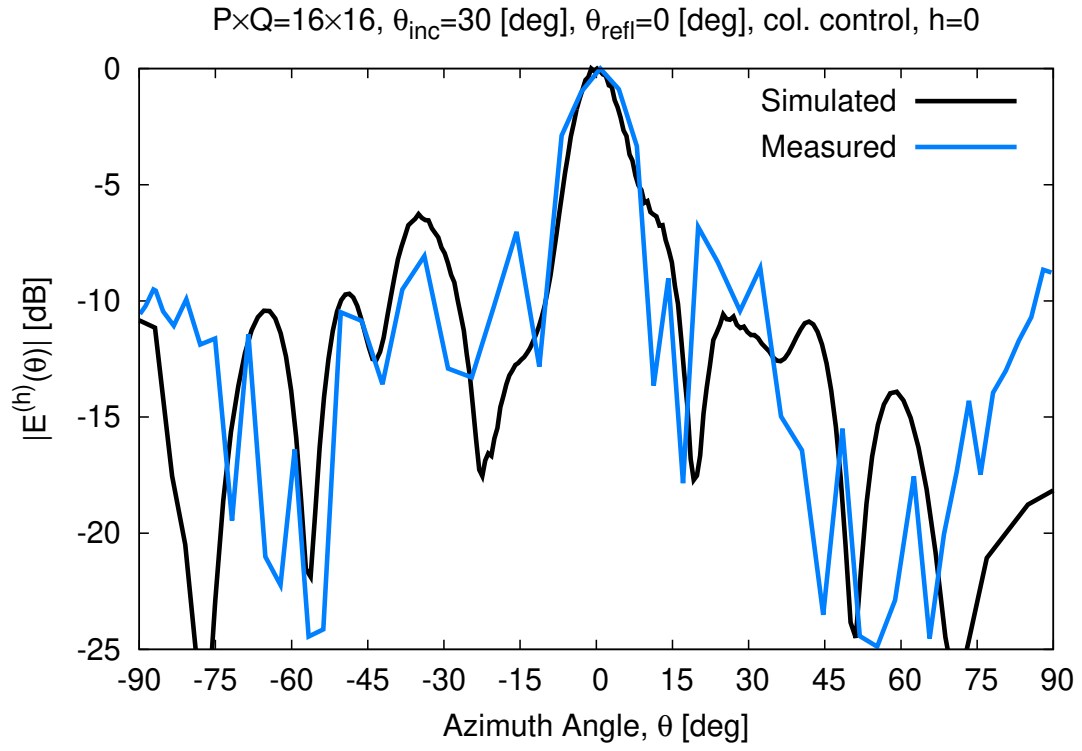


Fig. 15 - L. Poli *et al.*, “Time-Modulated EM Skins for Integrated ...”

Parameter	Value	Parameter	Value
g_1	35 [μm]	g_8	1.1 [mm]
g_2	1.6 [mm]	g_9	2.4 [mm]
g_3	15.2 [μm]	g_{10}	0.3 [mm]
g_4	0.1 [mm]	g_{11}	30 [deg]
g_5	0.2 [mm]	g_{12}	0.8 [mm]
g_6	12.6 [mm]	g_{13}	4.0 [mm]
g_7	2.0 [mm]	g_{14}	4.4 [mm]

Table I - L. Poli *et al.*, “Time-Modulated EM Skins for Integrated ...”